

Learning from geometry-aware near-misses to real-time COR: A spatiotemporal grouped random GEV framework

Mohammad Anis^a, Yang Zhou^{a,*} and Dominique Lord^a

^aZachry Department of Civil & Environmental Engineering, Texas A&M University, College Station, TX 77843, USA

ARTICLE INFO

Keywords:

Corridor-level crash risk
Pro-active safety
Short-term risk prediction
Vehicle dynamics
Near-miss
2D-TTC
Extreme value theory
Hierarchical Bayesian modeling
Autonomous vehicles

ABSTRACT

Real-time prediction of corridor-level crash occurrence risk (COR) remains challenging, as existing near-miss based extreme value models oversimplify collision geometry, exclude vehicle–infrastructure (V–I) interactions, and inadequately capture spatial heterogeneity in vehicle dynamics. This study introduces a geometry-aware two-dimensional time-to-collision (2D-TTC) indicator within a Hierarchical Bayesian spatiotemporal grouped random parameter (HBSGRP) framework using a nonstationary univariate generalized extreme value (UGEV) model to estimate short-term COR in urban corridors. High-resolution trajectories from the Argoverse-2 dataset, covering 28 locations along Miami’s Biscayne Boulevard, were analyzed to extract extreme near misses (V–V and V–I). The model incorporates dynamic variables and road features as covariates, with partial pooling across locations to address unobserved heterogeneity. The results show that the HBSGRP–UGEV framework outperforms fixed-parameter alternatives, reducing the DIC by up to 7.5% for V–V and 3.1% for V–I near-misses. Predictive validation using ROC–AUC confirms strong performance: 0.89 for V–V segments, 0.82 for V–V intersections, 0.79 for V–I segments, and 0.75 for V–I intersections. Model interpretation reveals that relative speed and distance dominate V–V risks at intersections and segments, with deceleration critical in segments, while V–I risks are driven by speed, boundary proximity, and steering/heading adjustments. These findings highlight the value of a statistically rigorous, geometry-sensitive, and spatially adaptive modeling approach for proactive corridor-level safety management, supporting real-time interventions and long-term design strategies aligned with Vision Zero.

1. Introduction

The increasing complexity of urban road networks, rising traffic volumes, and the coexistence of human-driven vehicles (HDVs) and autonomous vehicles (AVs) require innovative safety assessment approaches. Urban corridors are particularly vulnerable, where a single incident can disrupt mobility, trigger cascading congestion, and impose severe economic losses. In 2023, traffic crashes in the United States claimed 40901 lives, with a fatality rate of 1.26 per 100 million vehicle miles traveled (VMT) (National Center for Statistics and Analysis, 2025). The total annual cost of crashes is estimated to exceed \$1.85 trillion, including \$460 billion in direct economic losses and \$1.4 trillion in reduced quality of life (Blincoe et al., 2023). Despite extensive research on crash patterns, risk estimation, and mitigation strategies (Lanzaro et al., 2023; Kamel et al., 2023, 2024; Kamel and Sayed, 2024; Singh et al., 2024; Ghoul and Sayed, 2025; Singh et al., 2025; Anis et al., 2025b), accurate prediction of crash risk in urban corridors remains methodologically underdeveloped.

Most existing models focus exclusively on vehicle–vehicle (V–V) near-misses, largely due to the availability of vehicle trajectory data, while systematically excluding vehicle–infrastructure (V–I) interactions such as lane edges, curbs, barriers, and crosswalks. However, V–I events account for a substantial proportion of severe run-off-road and roadway departure crashes (Islam et al., 2021). This omission makes corridor-level safety models inherently incomplete. Recent advances in AV sensing and high-definition (HD) mapping, such as the Argoverse-2 dataset (Wilson et al., 2023), now allow the precise integration of roadway boundaries with vehicle trajectories, allowing both V–V and V–I near-misses to be modeled with geometric fidelity.

Crash risk prediction strategies based on historical retrospective crash data (Arun et al., 2021; Lee et al., 2017; Pei et al., 2011) suffer from well-documented limitations (Lord and Mannering, 2010; Lord et al., 2021; Mannering et al., 2020), including the rarity and stochastic nature of crashes, underreporting (Arun et al., 2021; Tarko, 2018),

*Corresponding author

✉ yangzhou295@tamu.edu (Yang Zhou)

temporal delays, and spatial mismatches with real-time conditions. These challenges motivate a paradigm shift towards proactive trajectory-based surrogate safety measures (SSMs) (Ali et al., 2023a; Arun et al., 2021; Mahmud et al., 2017). Using high-resolution vehicle trajectory data, SSMs reflect the underlying near-miss dynamics (Li et al., 2024; Tarko, 2018; Davis et al., 2011). Among SSMs, time-based indicators such as Time-to-Collision (TTC), Post-Encroachment Time (PET), and Modified TTC (MTTC) are widely used (Hayward, 1971; Perkins and Harris, (1967; Minderhoud and Bovy, 2001; Ozbay et al., 2008; Allen et al., 1978; Venthuruthiyil and Chunchu, 2022). However, these formulations often assume constant velocity and linear trajectories, leading to biased results in boundary-constrained environments. Recent research has extended TTC to two-dimensional (2D) indicators of higher-fidelity (Li et al., 2024; Anis et al., 2025b), incorporating latitude and longitude position, heading, and acceleration. However, even these advances typically employ simplified circular approximations, which can influence risk estimates in urban contexts where vehicle shape and alignment significantly influence the likelihood and severity of near misses. To support a reliable short-term crash occurrence risk (COR) estimate, SSM frameworks must enhance geometric fidelity to more accurately represent real-world interactions between vehicles and infrastructure. This study builds on these efforts by introducing a high-fidelity, geometry-aware 2D-TTC indicator that explicitly incorporates vehicle geometry, dynamic states, and roadway boundaries, ensuring realistic and efficient detection of both V–V and V–I near misses.

While SSMs capture frequent near-misses, a robust COR estimation framework requires extrapolating extreme near-misses to rare event outcomes. To date, several studies have proposed probabilistic (Saunier and Sayed, 2008), causal (Davis et al., 2011), and extreme value theory (EVT) (Fu and Sayed, 2021a,b; Zheng et al., 2021b; Ali et al., 2023a; Zheng et al., 2021a; Songchitruksa and Tarko, 2006; Zheng et al., 2014; Tarko, 2012). EVT provides a principled statistical foundation for this task, modeling the tail behavior of the extreme near-miss distribution. Two EVT approaches dominate: the Generalized Extreme Value (GEV) distribution using Block Maxima (BM) sampling and the Generalized Pareto Distribution (GPD) using Peaks over Threshold (POT) sampling (Coles et al., 2001). The BM approach is particularly suitable for real-time analysis due to its short block structure, lower threshold sensitivity, and compatibility with discrete-time samples (Fu and Sayed, 2022a).

Early applications of EVT in traffic safety employed stationary GEV models (Wang et al., 2018; Guo et al., 2019; Orsini et al., 2019; Alozi and Hussein, 2022; Hussain et al., 2022) that assumed constant parameterization across the study area. More recently, non-stationary GEV models have been introduced, allowing covariates to influence location and scale parameters (Tahir and Haque, 2024; Ali et al., 2022; Fu and Sayed, 2022a; Zheng et al., 2019; Nazir et al., 2023; Kar et al., 2024; Ali et al., 2023b; Alozi and Hussein, 2022; Zheng et al., 2014; Kar et al., 2023) and thereby capture heterogeneity across traffic states (Lanzaro et al., 2023; Kamel et al., 2023, 2024; Kamel and Sayed, 2024; Singh et al., 2024; Ghoul and Sayed, 2025; Singh et al., 2025; Anis et al., 2025b). Bayesian hierarchical extensions have also addressed data sparsity and unobserved heterogeneity (Zheng and Sayed, 2019; Fu and Sayed, 2022b). However, most applications remain geographically narrow and functionally limited to either intersections (Fu and Sayed, 2023, 2021c, 2022b) or segments (Kumar and Mudgal, 2024; Kamel et al., 2023; Kamel and Sayed, 2024; Anis et al., 2025b; Kamel et al., 2024). Although some studies have incorporated vehicle dynamics (Kumar and Mudgal, 2024; Fu and Sayed, 2022b; Anis et al., 2025b) and examined heterogeneity across traffic flow directions or roadway geometries (Kamel et al., 2023, 2024), these frameworks generally omit explicit integration of roadway geometry and directional heterogeneity at the corridor level. Such integration requires a modeling structure capable of jointly representing vehicle dynamics (which vary temporally) and roadway features (which vary spatially across segments and intersections). Therefore, a critical gap remains for a comprehensive Bayesian hierarchical GEV framework capable of jointly modeling vehicle dynamics, roadway geometry, flow directionality, and multilevel heterogeneity. This framework is crucial for accurately estimating the COR at the corridor level, which reflects the complex spatiotemporal dynamics of urban traffic environments. This paper makes the following unique contributions:

- Develops a corridor-level COR framework that simultaneously incorporates both V–V and V–I interactions, addressing a critical omission in previous studies.
- Introduces a geometry-aware high-fidelity 2D-TTC indicator that realistically captures extreme near-miss events by accounting for vehicle geometry, dynamic states, and roadway boundaries.
- Advances a hierarchical Bayesian spatiotemporal grouped random parameter (HBSGRP) Univariate GEV model that integrates roadway geometry, traffic flow directionality, and multilevel heterogeneity, enabling corridor-wide yet location-sensitive crash risk estimation

Together, these contributions establish the first infrastructure-aware, statistically rigorous framework for a proactive COR framework in urban corridors, leveraging Arogovers-2 AV trajectory and HD map data to support both operational interventions and long-term safety planning.

The remainder of this paper introduces the proposed 2D-TTC indicators, the HBSGRP–UGEV modeling framework, and the data preparation used in the analysis. This is followed by the presentation of model estimation, validation, and comparative results. The paper concludes with key findings, limitations, and directions for future research.

2. Near-miss detection framework

This section presents the modeling framework for computing a geometry-aware, high-fidelity 2D-TTC to support COR estimation. The framework integrates a continuous-time kinematic bicycle model, vehicle geometry representation, and a spatial near-miss detection algorithm, allowing capture of V-V and V-I interactions. Together, these components enable the accurate forecasting of vehicle trajectories and identification of potential near misses. The resulting architecture forms the computational backbone of the SSM analysis, ensuring a realistic representation of near-miss events in mixed-traffic environments.

2.1. Vehicle dynamics model

The vehicle dynamics module provides the predictive foundation of the framework. This adopts the kinematic bicycle model to represent vehicle footprint, as it is suitable for short-term near-miss analysis, where steering and acceleration dominate, and lateral slip can be neglected. The motion is represented by a four-dimensional (4D) dynamic state vector. At any time t , the state of vehicle i is given by:

$$\mathbf{x}_i(t) = \begin{bmatrix} x_i(t) \\ y_i(t) \\ \theta_i(t) \\ v_i(t) \end{bmatrix} \quad (1)$$

Here, $x_i(t)$, $y_i(t)$ denote the vehicle's global center coordinates, $\theta_i(t)$ its heading angle, and $v_i(t)$ its speed. Over the prediction window, each vehicle is assumed to maintain constant acceleration a_i and steering angle δ_i , simplifying short-horizon trajectory integration. The motion then follows the standard kinematic bicycle equations:

$$\dot{x}_i(t) = v_i(t) \cos \theta_i(t) \quad (2)$$

$$\dot{y}_i(t) = v_i(t) \sin \theta_i(t) \quad (3)$$

$$\dot{\theta}_i(t) = \frac{v_i(t)}{L_i} \tan \delta_i \quad (4)$$

$$\dot{v}_i(t) = a_i \quad (5)$$

Here, L_i is the vehicle wheelbase, influencing the turning radius and path curvature of vehicle i . The steering angle δ_i and acceleration a_i are treated as fixed inputs over the lookahead period. Equations (2-5) describe the rates of change in position, orientation, and velocity, determining the vehicle's trajectory. To model interactions, individual states are concatenated into an eight-dimensional (8D) joint state vector, defined as:

$$X(t) = \left[x_A(t) \quad y_A(t) \quad \theta_A(t) \quad v_A(t) \quad x_B(t) \quad y_B(t) \quad \theta_B(t) \quad v_B(t) \right]^T \quad (6)$$

The vector field that governs the evolution of this combined state is F defined as:

$$\dot{X}(t) = F(X(t)) = \left[v_A \cos \theta_A \quad v_A \sin \theta_A \quad \frac{v_A}{L_A} \tan \delta_A \quad a_A \quad v_B \cos \theta_B \quad v_B \sin \theta_B \quad \frac{v_B}{L_B} \tan \delta_B \quad a_B \right]^T \quad (7)$$

The state-space vector field in Eqn.7 gives the instantaneous rate of change of the joint state $\dot{X}(t)$. Its forward evolution is computed using the fourth-order Runge–Kutta (RK4) method, which balances accuracy and efficiency for nonlinear vehicle dynamics. The time horizon is discretized into N steps of size Δt ($t_n = n\Delta t$, $n = 0, 1, \dots, N$), and the RK4 update for state $X(t_{n+1})$ from $X(t_n)$ is:

$$X_{n+1} = X_n + \frac{\Delta t}{6} (k_1 + 2k_2 + 2k_3 + k_4) \quad (8)$$

where the intermediate slope evaluations $k_1, \dots, k_4 \in \mathbb{R}^8$ are defined as:

$$\begin{aligned} k_1 &= F(X_n) \\ k_2 &= F\left(X_n + \frac{\Delta t}{2}k_1\right) \\ k_3 &= F\left(X_n + \frac{\Delta t}{2}k_2\right) \\ k_4 &= F\left(X_n + \Delta t \cdot k_3\right) \end{aligned} \quad (9)$$

This integration is repeated for each timestep $n \in \{0, \dots, N-1\}$, producing a sequence of predicted states $\{X_n\}$ over the horizon. These trajectories form the basis for geometric collision checks between vehicles and roadway boundaries.

2.2. Vehicle geometry representation

Although the dynamic model predicts vehicle positions and headings, accurate near-miss detection requires a realistic representation of the vehicle footprint. Simplifying vehicles as points or circles often misrepresents interactions, especially during lane changes, swerving, or angled approaches. To address this, each vehicle is modeled as a rigid rectangle defined by its actual length L_i^{veh} and width W_i^{veh} (vehicle $i \in \{A, B\}$). The vehicle is centered at its center of gravity, with four corners specified in the body-fixed coordinate system as:

$$b_i^{(j)} = \begin{bmatrix} \xi_i^{(j)} \\ \eta_i^{(j)} \end{bmatrix}, \quad j = 1, 2, 3, 4 \quad (10)$$

where $\xi_i^{(j)} \in \left\{ +\frac{L_i^{\text{veh}}}{2}, -\frac{L_i^{\text{veh}}}{2} \right\}$ and $\eta_i^{(j)} \in \left\{ +\frac{W_i^{\text{veh}}}{2}, -\frac{W_i^{\text{veh}}}{2} \right\}$. This results in four corners: front-left, front-right, rear-left, and rear-right, expressed relative to the vehicle's center in the local frame.

To compute the position of each corner in the global coordinate frame at time t , the body-fixed corner coordinates are first rotated by the vehicle's heading angle $\theta_i(t)$, and then translated by the vehicle's center position $(x_i(t), y_i(t))$. This transformation is written as:

$$p_i^{(j)}(t) = \begin{bmatrix} x_i(t) \\ y_i(t) \end{bmatrix} + R(\theta_i(t)) \cdot b_i^{(j)} \quad (11)$$

where $R(\theta_i(t))$ is the 2D rotation matrix defined as:

$$R(\theta_i(t)) = \begin{bmatrix} \cos \theta_i(t) & -\sin \theta_i(t) \\ \sin \theta_i(t) & \cos \theta_i(t) \end{bmatrix} \quad (12)$$

This transformation rotates the local corner coordinates by the heading angle and translates them into the global frame. Repeating it for all corners at each timestep produces the vehicle's time-varying geometric footprint, which serves as input for near-miss detection. These footprints enable precise evaluation of proximity-based events, both V-V and V-I, ensuring accurate 2D-TTC estimation while reducing false positives from geometric simplifications.

2.3. V-V near-miss detection

Vehicles are modeled as rigid rectangles, and their interactions are determined by predicted states and orientations. At each timestep of the RK4 integration, the global positions of all four corners are computed using the kinematic and rotational transformations. A collision is defined when a vehicle's corner lies within a proximity threshold of a corner of another vehicle. Let $p_A^{(j)}(t)$ and $p_B^{(k)}(t)$ denote the global coordinates of corners j and k of vehicles A and B at time t . A V-V near-miss is flagged if any pair of these corners satisfies the proximity condition.

$$p_A^{(j)}(t) = p_B^{(k)}(t) \quad (13)$$

An exact match between corners of two vehicles is highly unlikely due to floating-point arithmetic and continuous motion. Instead, a practical criterion is applied: a collision is flagged if the difference in both the x and y coordinates of any corner pair is less than or equal to a small threshold ϵ :

$$|x_A^{(j)} - x_B^{(k)}| \leq \epsilon \quad (14)$$

$$|y_A^{(j)} - y_B^{(k)}| \leq \epsilon \quad (15)$$

The rotation-translation transformation from each vehicle's center and heading angle gives the global corner coordinates, for vehicles A and B:

$$x_A^{(j)} = x_A + \xi_A^{(j)} \cos \theta_A - \eta_A^{(j)} \sin \theta_A \quad (16)$$

$$y_A^{(j)} = y_A + \xi_A^{(j)} \sin \theta_A + \eta_A^{(j)} \cos \theta_A \quad (17)$$

$$x_B^{(k)} = x_B + \xi_B^{(k)} \cos \theta_B - \eta_B^{(k)} \sin \theta_B \quad (18)$$

$$y_B^{(k)} = y_B + \xi_B^{(k)} \sin \theta_B + \eta_B^{(k)} \cos \theta_B \quad (19)$$

At each timestep, all 16 corner-pair combinations are evaluated. A V-V near-miss is flagged if any pair satisfies the proximity condition, and the corresponding collision time t_c is recorded for 2D-TTC computation. This discrete-time approach enables accurate detection of spatial overlap while avoiding the oversimplifications of circular vehicle approximations.

2.4. V-I near-miss detection

In addition to V-V interactions, the framework also detects near misses between vehicles and roadway infrastructure, including curbs, medians, or barriers. Capturing these V-I events is critical for identifying edge encroachments or departures that often precede run-off-road crashes.

Road boundaries are represented as static polylines of M discrete points (X_ℓ, Y_ℓ) consistent with HD map formats in datasets such as Argoverse-2. At each timestep, the global positions of the four vehicle corners $p_i^{(j)}(t)$ are obtained from the predicted state. The distance between a vehicle corner j and boundary point ℓ , the distance at time t is computed as:

$$d_{j,\ell}(t) = \sqrt{(x^{(j)}(t) - X_\ell)^2 + (y^{(j)}(t) - Y_\ell)^2} \quad (20)$$

A near-miss is flagged if $d_{j,\ell}(t) \leq \epsilon$ for any corner and boundary point, where ϵ is a proximity threshold accounting for numerical tolerances. When this occurs, the corresponding time t_c is recorded as the instant of boundary contact. These events are then passed to the 2D-TTC framework to support extreme risk estimation.

2.5. Spatiotemporal COR

The near-miss detection framework integrates vehicle dynamics, geometric transformations, and spatial proximity checks to identify both V-V and V-I events. Forward trajectories are simulated using RK4 integration, vehicle corners are transformed into global coordinates, and geometric overlaps are evaluated to detect potential near-misses across the

Algorithm 1: Near-miss detection based on state integration and geometric overlap

Input: Initial state $\mathbf{X}(0)$, vehicle parameters $l_i, L_i^{\text{veh}}, W_i^{\text{veh}}$, control inputs a_i, δ_i , and boundary points $\{(X_\ell, Y_\ell)\}$

Output: Earliest collision time t_c

```
1 for each timestep  $n = 0$  to  $N - 1$  do
2   Simulate  $\mathbf{X}_n \rightarrow \mathbf{X}_{n+1}$  using RK4 integration;
3   Compute global corner positions  $\mathbf{p}_i^{(j)}$  for each vehicle;
4   for each corner pair  $(j, k) \in \{1, 2, 3, 4\}^2$  do
5     if  $|x_A^{(j)} - x_B^{(k)}| \leq \varepsilon$  or  $|y_A^{(j)} - y_B^{(k)}| \leq \varepsilon$  then
6       Record V-V near-miss, set  $t_c$ ;
7   for each corner  $j$  and boundary point  $\ell$  do
8     Compute  $d_{j,\ell}(t) = \sqrt{(x^{(j)} - X_\ell)^2 + (y^{(j)} - Y_\ell)^2}$ ;
9     if  $d_{j,\ell}(t) \leq \varepsilon$  then
10      Record V-I near-miss, set  $t_c$ ;
11 return the earliest collision time  $t_c$  as 2D-TTC
```

prediction horizon. The procedure is summarized in Algorithm 1, and a conceptual illustration is provided in Fig. 1. These steps yield a time series of 2D-TTC values for each interaction block.

While this geometric framework enables precise localization of near misses, it does not capture the probabilistic structure or temporal evolution of COR. To address this, the extracted blockwise minima of 2D-TTC are modeled using the EVT model. For each block, the model estimates the probability that 2D-TTC falls below a critical safety threshold, which defines the COR metric as a short-term indicator of crash risk. Block duration is chosen to balance temporal sensitivity with statistical stability across diverse contexts. This framework, therefore, combines deterministic near-miss detection with probabilistic EVT modeling to enable localized, data-driven assessment of crash-prone conditions. The complete methodological pipeline, from trajectory simulation to dynamic risk estimation, is summarized in Fig. 2.

3. Extreme value theory (EVT)

Extreme Value Theory (EVT) provides the statistical foundation for estimating COR by extrapolating rare, high-severity events from frequent near-misses. In this study, extreme events are represented by block maxima of 2D-TTC derived from high-resolution vehicle trajectories (Algorithm 1). EVT allows risk estimation without requiring large volumes of historical crash data (Zheng and Sayed, 2020; Fu and Sayed, 2022a). Two EVT approaches are commonly applied: the Block Maxima (BM) method, which fits maxima or minima from fixed-duration blocks using the Generalized Extreme Value (GEV) distribution (Coles et al., 2001), and the Peaks Over Threshold (POT) method, which models threshold exceedances using the Generalized Pareto Distribution (GPD). Although POT can be data-efficient, it is highly sensitive to threshold choice and less compatible with discrete sensor-derived datasets. By contrast, BM aligns naturally with real-time AV data, avoids subjective thresholds, and supports scalable, time-series analysis (Fu and Sayed, 2022a; Songchitruksa and Tarko, 2006). Consequently, this study adopts the BM-GEV framework (see Fig. 2).

The GEV has been widely applied in traffic safety research. Early studies modeled near-misses with univariate and multivariate GEV formulations (Orsini et al., 2020; Zhang et al., 2019; Zheng et al., 2014). Recent advances incorporate nonstationary structures, linking GEV parameters to covariates such as vehicle dynamics (Anis et al., 2025b; Fu and Sayed, 2021c, 2022b). Bayesian hierarchical models have also addressed sparse data and unobserved heterogeneity across vehicles, sites, and traffic contexts. The increasing availability of high-resolution AV trajectory and HD map data has highlighted the need for flexible GEV formulations that jointly capture V-V and V-I interactions.

Despite this progress, most UGEV models still neglect the joint influence of roadway geometry and vehicle dynamics, two critical but distinct sources of heterogeneity. Roadway geometry (e.g., lane count, curvature, median type) is spatially structured and relatively stable within segments or intersections, while vehicle dynamics (e.g., speed, acceleration) vary temporally and spatially, driving short-term behavioral volatility. Capturing this multilevel

heterogeneity is crucial for estimating corridor and network level crash risk. To address this gap, this study develops a hierarchical Bayesian Spatiotemporal Grouped Random Parameter (HBSGRP) UGEV model. Unlike standard random-parameter models, which assign variation independently to each unit, grouped random parameters capture shared variation across clusters (e.g., segment types, corridor directions) while allowing for within-group variability. This structure provides both flexibility and parsimony, making it well-suited for high-resolution, corridor-scale crash risk modeling (Washington et al., 2020; Cai et al., 2018; Islam et al., 2023).

3.1. Univariate generalized extreme value (UGEV)

As established in the previous section, the BM-based UGEV model is employed to characterize the tail behavior of 2D-TTC, which represents the most critical near-miss events in both V–V and V–I interactions. To implement this framework, continuous vehicle trajectories are partitioned into fixed-duration windows (e.g., 11 s). Within each window, the minimum 2D-TTC is extracted and negated, consistent with the upper-tail modeling convention of UGEV (Coles et al., 2001). The resulting sequence of BM serves as the input for parameter estimation. Throughout this study, we focus on maxima, denoted as M_n , under the assumption that each block consists of n independent and identically distributed (i.i.d.) random variables, X_1, X_2, \dots, X_n . To align with conventional UGEV formulations, we consider the negative values of the original variables derived from Algorithm 1, thereby defining the block maximum as $M_n = \max\{-X_1, -X_2, \dots, -X_n\}$. Under suitable regularity conditions, if there exist sequences of constants $a_n \in \mathbb{R}$ and $b_n > 0$, the normalized block maxima $M_n^* = (M_n - a_n)/b_n$ converge in distribution to a non-degenerate limit $G(x)$ as $n \rightarrow \infty$, then: $\Pr\left(\frac{M_n - a_n}{b_n} \leq X\right) \xrightarrow{n \rightarrow \infty} f(x)$, where $G(x)$ is a non-degenerate distribution function. According to EVT, the limiting distribution $G(x)$ must belong to one of three families: Gumbel, Fréchet, or Weibull, each of which can be captured by the parametric form of the GEV distribution (Coles et al., 2001). Let the UGEV be defined as:

$$G(x; \mu_x, \sigma_x, \xi_x) = \exp \left\{ - \left[1 + \xi_x \left(\frac{x - \mu_x}{\sigma_x} \right) \right]^{-1/\xi_x} \right\}, \quad \text{where } 1 + \xi_x \left(\frac{x - \mu_x}{\sigma_x} \right) > 0 \quad (21)$$

Here, $\mu_x \in \mathbb{R}$ is the location parameter, $\sigma_x > 0$ the scale, and $\xi_x \in \mathbb{R}$ the shape. The value of ξ_x determines tail heaviness: $\xi_x > 0$ corresponds to the heavy-tailed Fréchet, $\xi_x < 0$ to the bounded Weibull, and $\xi_x = 0$ to the light-tailed Gumbel case.

3.1.1. Hierarchical Bayesian Spatiotemporal Grouped Random Parameter (HBSGRP) model

To capture structured heterogeneity in extreme outcomes across the corridor, we employ a Hierarchical Bayesian Spatiotemporal Grouped Random Parameter (HBSGRP) model. Unlike conventional random-parameter models that assign variation to individual units, the HBSGRP formulation introduces variation at the group level. This structure allows systematic differences across predefined observational groups while maintaining parsimony and interpretability. In this specification, covariates are divided into two sets: fixed effects X , which apply uniformly across all observations, and group-varying effects Z , whose coefficients differ across groups. For a dataset divided into K groups, with observations i belonging to group $k(i)$, both the intercept and selected slopes are allowed to vary by group. This enables the capture of localized relationships while preserving overall model coherence. The model is expressed within a three-layer hierarchical Bayesian framework. The data layer specifies the likelihood of observed block maxima of 2D-TTC from V–V and V–I interactions, assuming a UGEV distribution. The process layer links covariates to UGEV parameters through fixed and group-level random effects, with optional latent terms (e.g., Gaussian processes) to capture residual spatial–temporal dependence. The prior layer defines prior distributions for all parameters and hyperparameters, supporting regularization and uncertainty quantification.

Bayesian inference proceeds by updating prior beliefs with observed data to obtain the posterior distribution. Formally, the joint posterior of parameters Θ , given data X , is:

$$q(\Theta | X) \propto q_{\text{data}}(X | \Theta) \cdot q_{\text{process}}(\Theta | \Psi) \cdot q_{\text{prior}}(\Psi) \quad (22)$$

In this formulation, $q(\Theta | X)$ denotes the posterior distribution, integrating both the data likelihood and prior knowledge. The term $q_{\text{data}}(X | \Theta)$ corresponds to the likelihood function defined by the EVT assumptions. The component $q_{\text{process}}(\Theta | \Psi)$ captures the hierarchical dependency structure, including the group-varying parameters.

Lastly, $q_{\text{prior}}(\Psi)$ encompasses the prior distributions of hyperparameters that control the model's flexibility and penalize over-complexity.

The likelihood function for the data layer is specified as each extreme value sample $X_{k,i}$, observed for event i within group K , is modeled as:

$$q_{\text{data}}(X_{k,i} | \Theta) = \prod_{k=1}^K \prod_{i=1}^{N_k} \frac{1}{\sigma_{k,i}} \exp \left\{ - \left[1 + \xi_{k,i} \left(\frac{X_{k,i} - \mu_{k,i}}{\sigma_{k,i}} \right) \right]^{-1/\xi_{k,i}} \right\} \left[1 + \xi_{k,i} \left(\frac{X_{k,i} - \mu_{k,i}}{\sigma_{k,i}} \right) \right]^{-1-1/\xi_{k,i}} \quad (23)$$

The location ($\mu_{k,i}$), scale ($\sigma_{k,i}$), and shape ($\xi_{k,i}$) parameters are expressed as functions of group-level fixed-effect covariates $X_{k,j}$ (e.g., road geometry, speed limit) and sample-specific random-effect covariates $W_{k,i,j}$ (e.g., speed, acceleration, time-to-collision) as follows:

$$\mu_{k,i} = \beta_{\mu,0} + \sum_{j=1}^J \beta_{\mu,j} X_{k,j} + \sum_{j=1}^{J'} \gamma_{\mu,j,k} W_{k,i,j} \quad (24)$$

$$\vartheta_{k,i} = \beta_{\sigma,0} + \sum_{j=1}^J \beta_{\sigma,j} X_{k,j} + \sum_{j=1}^{J'} \gamma_{\sigma,j,k} W_{k,i,j}, \quad \sigma_{k,i} = \exp(\vartheta_{k,i}) \quad (25)$$

$$\xi_{k,i} = \beta_{\xi,0} + \sum_{j=1}^J \beta_{\xi,j} X_{k,j} \quad (26)$$

In the above equations, $X_{k,j}$ defined as a group-level fixed-effect covariate j , $W_{k,i,j}$ is a sample-specific random-effect covariate j . $\beta_{\mu,0}, \beta_{\sigma,0}, \beta_{\xi,0}$ as fixed intercepts for respective parameters. $\beta_{\mu,j}, \beta_{\sigma,j}, \beta_{\xi,j}$: fixed-effect coefficients. $\gamma_{\mu,j,k}, \gamma_{\sigma,j,k}$: random-effect coefficients, varying across groups k . Therefore, the likelihood for the process layer, modeling within-group variability, is defined as:

$$q_{\text{process}}(\Theta | \Psi) = \prod_{k=1}^K \prod_{i=1}^{N_k} \frac{1}{\sqrt{2\pi\tau_{\mu}^2}} \exp \left\{ -\frac{1}{2\tau_{\mu}^2} (\mu_{k,i} - \bar{\mu}_k)^2 \right\} \\ \times \frac{1}{\sqrt{2\pi\tau_{\vartheta}^2}} \exp \left\{ -\frac{1}{2\tau_{\vartheta}^2} (\vartheta_{k,i} - \bar{\vartheta}_k)^2 \right\} \times \frac{1}{\sqrt{2\pi\tau_{\xi}^2}} \exp \left\{ -\frac{1}{2\tau_{\xi}^2} (\xi_{k,i} - \bar{\xi}_k)^2 \right\} \quad (27)$$

where $\bar{\mu}_k, \bar{\vartheta}_k$, and $\bar{\xi}_k$ are group-specific average parameters.

Prior distributions are assigned to all model parameters. The priors for fixed and random effect coefficients are as follows:

$$q_{\text{prior}}(\Psi) = q_{\beta_{\mu,0}}(\beta_{\mu,0}) \cdot \prod_{j=1}^J q_{\beta_{\mu,j}}(\beta_{\mu,j}) \cdot \prod_{k=1}^K \prod_{j=1}^{J'} q_{\gamma_{\mu,j,k}}(\gamma_{\mu,j,k}) \\ \times q_{\beta_{\sigma,0}}(\beta_{\sigma,0}) \cdot \prod_{j=1}^J q_{\beta_{\sigma,j}}(\beta_{\sigma,j}) \cdot \prod_{k=1}^K \prod_{j=1}^{J'} q_{\gamma_{\sigma,j,k}}(\gamma_{\sigma,j,k}) \times q_{\beta_{\xi,0}}(\beta_{\xi,0}) \cdot \prod_{j=1}^J q_{\beta_{\xi,j}}(\beta_{\xi,j}) \quad (28)$$

Hyperpriors for the variance parameters $\tau_{\mu}^2, \tau_{\vartheta}^2, \tau_{\xi}^2$ are modeled using inverse gamma distributions:

$$\tau_{\mu}^2 \sim \text{IG}(\alpha_{\mu}, \beta_{\mu}), \quad \tau_{\vartheta}^2 \sim \text{IG}(\alpha_{\vartheta}, \beta_{\vartheta}), \quad \tau_{\xi}^2 \sim \text{IG}(\alpha_{\xi}, \beta_{\xi}) \quad (29)$$

where $\text{IG}(\alpha, \beta)$ denotes an inverse gamma prior distribution ensuring positivity constraints for variance parameters.

3.2. COR estimation

Building on the HBSGRP–UGEV estimates, the framework computes COR by evaluating the probability that 2D-TTC for both V–V and V–I interactions falls below a critical threshold within each block. Unlike severity-stratified approaches, this framework estimates the total number of latent extreme near-miss events regardless of outcome severity, allowing for a holistic assessment of potential COR under mixed traffic conditions.

Let k, i denote the block i within the group k , where groups correspond to spatial or functional corridor classifications (e.g., intersections or directional segments). The minimum 2D-TTC in each block is modeled with the HBSGRP-UGEV distribution, parameterized by $\mu_{k,i}$, $\sigma_{k,i}$, and $\xi_{k,i}$. Let ω be the critical 2D-TTC threshold below which a near-miss is considered crash-prone. The probability of a crash-level event in block i of group k is:

$$P_{k,i}^{\text{crash}} = \Pr(2D\text{-}TTC_{k,i} \leq \omega) = 1 - \exp \left\{ - \left[1 - \xi_{k,i} \left(\frac{\omega - \mu_{k,i}}{\sigma_{k,i}} \right) \right]^{-1/\xi_{k,i}} \right\}, \quad \text{where } 1 - \xi_{k,i} \left(\frac{\omega - \mu_{k,i}}{\sigma_{k,i}} \right) > 0 \quad (30)$$

Assuming a homogeneous Poisson process for exceedances, the expected COR for the group k is obtained by aggregating exceedance probabilities across blocks and normalizing by exposure duration T . Here $y_{k,i}$ is the number of near-misses (V-V or V-I) in block i , and N_k the number of blocks in group k . The expected COR for group k is:

$$COR_k = \frac{1}{T} \sum_{i=1}^{N_k} y_{k,i} \cdot P_{k,i}^{\text{crash}} = \frac{1}{T} \sum_{i=1}^{N_k} y_{k,i} \cdot \left[1 - \exp \left\{ - \left[1 - \xi_{k,i} \left(\frac{\omega - \mu_{k,i}}{\sigma_{k,i}} \right) \right]^{-1/\xi_{k,i}} \right\} \right] \quad (31)$$

The total expected crash frequency across the study area is then:

$$C_{F_{\text{total}}} = \sum_{k=1}^K COR_k = \frac{1}{T} \sum_{k=1}^K \sum_{i=1}^{N_k} y_{k,i} \cdot \left[1 - \exp \left\{ - \left[1 + \xi_{k,i} \left(\frac{\omega - \mu_{k,i}}{\sigma_{k,i}} \right) \right]^{-1/\xi_{k,i}} \right\} \right] \quad (32)$$

This formulation integrates exceedance probabilities from the HBSGRP–UGEV model with observed V–V and V–I near-miss counts, maintaining a direct link between real-world interaction intensity and modeled crash propensity. By separating probability from exposure, the framework yields interpretable, proactive crash frequency estimates aligned with EVT-based safety assessment.

4. Data description

The effectiveness of real-time COR estimation is critically dependent on the fidelity and coverage of trajectory data. Traditional sensing technologies, such as roadside cameras, loop detectors, and fixed LiDAR, have supported safety analysis by capturing speed, spacing, and acceleration patterns (Islam et al., 2021; Yuan et al., 2019; Li et al., 2020). However, these systems suffer from narrow fields of view, occlusion, overlapping detections, and high maintenance costs, which limit scalability and data quality (St-Aubin et al., 2013). Recent advances in AV sensing offer a promising alternative. AV datasets provide high-frequency, multimodal trajectories with unprecedented spatial precision, allowing for detailed analysis of kinematics, spacing, and maneuvers. This richness allows for realistic near-miss detection in complex traffic environments. Despite this potential, AV data remain underutilized in generalized frameworks for real-time COR estimation. For example, studies using the Waymo Open Dataset have focused mainly on localized near-miss events without incorporating roadway geometry or V-I interactions, limiting broader applicability (Anis et al., 2025b).

To address these challenges, this study uses the Argoverse-2 dataset (Wilson et al., 2023), which was collected in 2021 across six U.S. cities (Austin, Detroit, Miami, Palo Alto, Pittsburgh, and D.C.) using SAE Level 4 AVs. Argoverse-2 comprises more than 250k driving scenarios that span 113 roadway segments, with each 11-second scenario sampled at 10 Hz. Compared to Waymo Open (Ettinger et al., 2021), Lyft Level-5 (Houston et al., 2021), and nuScenes (Caesar et al., 2020), Argoverse-2 is uniquely curated to emphasize safety-critical interactions, such as intersection near-misses, lane changes, and pedestrian crossings, conditions most indicative of crash risk. A defining feature of Argoverse-2 is its scene-adaptive sampling, which prioritizes high-interaction episodes rather than routine free-flow traffic. Scenarios are annotated with agent IDs, AV driving mode, and map-relative lane-following behaviors. The sensor suite includes

Table 1

Representative open-source AV datasets with applications in safety and crash-risk analysis

Dataset	Trajectory coverage ^a	Safety relevance ^b	Duration / Frequency	HD map	Notes
Argoverse-2	250k scenarios; 113 segments; 6 cities	Near-miss analysis, surrogate safety measures	11s per scenario, 10 Hz	Yes	Rich lane-level geometry; 10 object classes (Wilson et al. 2023)
nuScenes	40k scenes; ~1000 segments; 2 cities	Multi-agent interactions, trajectory risk indicators	20s per scene, 2 Hz	No	23 object classes; widely used urban dataset (Caesar et al. 2020)
Waymo	390k scenarios; ~1950 segments; 6 cities	Motion forecasting, crash-prone interaction detection	Up to 20s, 10 Hz	Yes	12.6M trajectories across diverse geometries (Ettinger et al. 2021)
Lyft Level 5	170k instances; 1 city	Vehicle interactions; trajectory-based safety studies	25s per instance, 10 Hz	Yes	Limited geographic diversity; 10 object classes (Kesten et al. 2019)
KITTI	15k scenes; 1 city	Early surrogate measures, safety benchmarks	1–2 min sequences, 10 Hz	No	Classic full-stack dataset, still widely cited (Geiger et al. 2013)
DAIR-V2X	71k frames	Infrastructure-based safety monitoring	–	Yes	First large-scale real-world V2X dataset (Yu et al. 2022)
OPV2V	33k samples; CARLA simulation	Cooperative perception, proactive safety design	10 Hz	No	18k V2X frames, sim environment (Xu et al. 2022)
DeepAccident	285k samples; sim dataset	Rare crash/near-crash events, proactive safety	10 Hz	Yes	Includes 57k V2X scenarios (Wang et al. 2024)
Shift	2.5M frames; 4850 segments; 8 cities	Long-term safety and mobility analysis	10 Hz	No	Corridor-scale benchmarking dataset (Sun et al., 2022)

^a **Trajectory coverage:** Number of driving scenarios and geographic spread.

^b **Safety relevance:** Potential application for crash risk, near-miss, or surrogate safety studies.

seven ring cameras and two front-facing stereo cameras (20 Hz) supported by dual 64-beam VLP-32C LiDAR sensors, producing 107k 3D points per frame. HD maps contain lane centerlines, crosswalks, medians, and drivable areas registered to local coordinates.

Argoverse-2 was selected after benchmarking open-source AV datasets (Table 1). Waymo Open offers a greater total mileage but lower near-miss density and no AV-behavior labels. Lyft Level-5 is confined to a single city and lacks scene-level filtering. nuScenes samples at 2 Hz, limiting the capture of rapid interactions. In contrast, Argoverse-2 balances spatial coverage, sensor fidelity, near-miss-rich scenarios, and behavioral annotations, making it well-suited to this study’s goals. This study used motion-forecasting and HD-map modules of Argoverse-2 to extract vehicle trajectories, compute near-miss indicators, and encode roadway geometry.

4.1. Data Preprocessing

To operationalize the proposed framework, both the motion forecasting and HD map modules of the Argoverse-2 dataset were processed through a structured pipeline. The preprocessing consisted of four key stages: (i) extraction of multi-agent trajectories, (ii) transformation of coordinates from local map space to global geographic space, (iii) integration with HD map features to contextualize V-I interactions, and (iv) selection of a high-risk urban corridor for detailed analysis.

4.1.1. Motion forecasting dataset

Each motion forecasting scenario follows a hierarchical structure with three levels: scenario metadata, agent tracks, and frame-level states. Scenarios are 11s duration and are sampled at 10 Hz, producing 110 time steps per vehicle for fine-grained interaction modeling. At the scenario level, metadata include a unique scenario ID, the recording city, and the focal agent, typically the ego AV. Each scenario then contains multiple agent tracks, where each track

corresponds to a road user and specifies the object type (e.g., vehicle, pedestrian, cyclist), scoring category (focal, scored, or unscored), and a time-ordered sequence of states. Frame-level states capture position, velocity, and heading at each timestep, forming the basis for computing 2D-TTC.

To implement the framework, we developed a Python-based batch pipeline using the Argoverse-2 SDK. The pipeline parsed motion forecasting scenarios across all cities and extracted tracks for all agents—not just the focal vehicle—to retain critical multi-agent interactions. For each track, frame-level kinematic attributes were retrieved, including (x, y) position, heading, velocity components, and timestamps.

Because positions were reported in local, city-specific frames, all coordinates were transformed to globally referenced WGS84. This involved (i) projecting each city's local origin into its UTM zone (e.g., Zone 17 for Miami, Pittsburgh, and Detroit), and (ii) offsetting local (x, y) positions and inverse-projecting them to latitude–longitude using `pyproj`. This geospatial normalization provided consistent referencing across cities and ensured compatibility with HD map overlays. Batch scripts automatically traversed scenario folders, performed attribute extraction and coordinate conversion, and exported unified CSV datasets containing both original city-frame and converted lat/lon values. These datasets were then used for spatial filtering, interaction detection, and overlay validation.

The processed files formed the basis for V–V and V–I near-miss detection. For each valid scenario, pairwise distances and relative approach rates were computed for all vehicle pairs, while V–I distances were derived from buffered polygons of lane edges and curbs in the HD map. Scenarios with no substantive interaction (e.g., straight-lane cruising without lane changes or turns) were excluded, ensuring the dataset emphasized behaviorally informative, high-risk conditions consistent with proactive safety modeling. Non-vehicle agents (e.g., pedestrians, cyclists) were also excluded at this stage, though the pipeline is extensible to incorporate vulnerable road users in future work.

4.1.2. HD map

The Argoverse-2 HD map dataset provides vectorized representations of roadway geometry and drivable space, enabling infrastructure-aware risk estimation. These maps are distributed as JSON files in local city coordinates and contain lane centerlines, left/right boundaries, crosswalk polygons, and drivable area definitions.

Lane-level geometry was extracted using the official Argoverse-2 API. The `get_all_lane_segments()` method returns centerline polylines along with left/right boundaries that define the navigable road space. Additional features, such as crosswalk polygons and drivable area masks, were also retrieved to support validation and visualization, though only lane boundaries and centerlines were directly used in near-miss detection.

Because all coordinates are expressed in city-specific Cartesian frames, global georeferencing was required to align HD maps with trajectory data. For each city, the WGS84 geodetic origin was projected into its respective UTM zone (e.g., Zone 17 for Miami and Pittsburgh, Zone 14 for Austin, Zone 10 for Palo Alto, Zone 18 for Washington, D.C.) using the `pyproj` library. Each local (x, y) coordinate was then offset by this origin and inverse-projected into latitude–longitude, ensuring spatial consistency across cities. Once transformed, all HD map components: lane boundaries, centerlines, and crosswalks—were indexed using their global coordinates and converted into shapefiles or GeoPandas geometries. This geospatial transformation enabled efficient spatial querying, collision proximity analysis, and visual overlay with satellite imagery and trajectory data. In particular, the lane boundaries were instrumental in detecting V–I near-misses by allowing for the computation of lateral vehicle encroachments beyond the legal driving space. From the processed dataset, a high-density urban corridor in Miami was present to showcase the transformation (see Fig. 3). This illustrates the transformation of AV data into real-world coordinates, its alignment with HD maps and satellite imagery, and the resulting traffic patterns that highlight interaction hotspots across intersections and midblocks.

4.1.3. Trajectory preprocessing and derivation of vehicle dynamics

Before computing 2D-TTC, a series of preprocessing steps was applied to ensure the precision, continuity, and physical plausibility of vehicle motion data from the Argoverse-2 dataset. These steps included the extraction of raw trajectory data, trajectory smoothing and filtering, and the derivation of dynamic variables such as speed, acceleration, and steering angle. First, all multi-agent trajectories were transformed from local city-specific frames to global WGS84 coordinates, enabling consistent alignment with HD map geometries. Raw trajectories were then examined for noise caused by sensor jitter, occlusion, or missed detections—issues more common in human-driven vehicles than in AV tracks. To suppress such noise while preserving curvature and lane-change dynamics, cubic B-spline smoothing was applied to the position coordinates (Eilers and Marx, 1996; Choi et al., 2024). This method effectively removed local fluctuations while retaining key geometric features (see Fig. 4). Stationary or irrelevant agents, such as parked vehicles and bicycles, were filtered out to reduce computational load and focus only on interaction-relevant entities.

Dynamic control inputs were then computed. Instantaneous speed v_t was derived as the Euclidean norm of velocity components:

$$v_t = \sqrt{v_{x,t}^2 + v_{y,t}^2} \quad (33)$$

Residual noise in v_t was suppressed with a Savitzky–Golay filter (Chen et al., 2004) using a second-order polynomial and a 110-frame window (11s). Longitudinal acceleration (a_t) was obtained by first-order numerical differentiation:

$$a_t = \frac{v_{t+1} - v_t}{\Delta t} \quad (34)$$

where $\Delta t = 0.01$ s reflects the 10 Hz sampling rate. Heading θ_t was computed from directional vectors of each track and was unwrapped to maintain continuity across discontinuities at $\pm\pi$. The yaw rate $\dot{\delta}_t$ was derived from the kinematic bicycle model:

$$\dot{\theta}_t = \frac{\theta_{t+1} - \theta_t}{\Delta t} \quad (35)$$

$$\delta_t = \tan^{-1} \left(\frac{L \cdot \dot{\theta}_t}{v_t} \right) \quad (36)$$

The final dataset included per-frame values of speed, acceleration, heading, yaw rate, and steering angle for each track, providing stable and interpretable control inputs. These preprocessed trajectories formed the basis for subsequent near-miss detection using Algorithm 1 and the HBSGRP-UGEV model.

4.2. Study area

Under realistic and heterogeneous urban traffic conditions, a representative high-volume corridor was selected along Biscayne Boulevard in Miami, Florida. This arterial extends from Downtown Miami through the Upper East Side toward the northern city limits, serving as a critical connector to major activity centers, including the Miami International Airport region. It is characterized by multimodal interactions, geometric complexity, frequent turning maneuvers, and diverse traffic control features. The corridor was chosen for its rich coverage in the Argoverse-2 motion forecasting dataset, HD map, and its suitability for extracting sufficient samples for extreme near-miss scenarios.

As shown in Fig. 5, the study area was extracted using ArcGIS Pro based on scenario density, HD map fidelity, and heterogeneity of vehicle maneuvers. The extracted network includes a continuous corridor with multiple intersections, midblock segments, and bidirectional traffic operations. For analytical consistency, the corridor was subdivided into nine directional segments (S1–S9) and ten intersections (I1–I10). Segment boundaries were defined midblock to maintain flow continuity, while intersections were delineated to capture near-miss-prone zones such as turning paths, crosswalks, and lane merges. Each subregion was mapped with lane boundaries, crosswalks, and vehicle trajectories to preserve geometric fidelity and directional alignment. Insets in Fig. 5 illustrate the spatial configuration of the segmented units, which serve as the basis for grouped modeling and localized risk estimation.

Table 2 provides a detailed profile of the 28 study subregions, consisting of 10 intersections and 18 directional segments. Intersections generally show fewer scenarios and unique vehicles (e.g., I2 with 47 scenarios and 220 vehicles, I4 with 96 scenarios and 568 vehicles) compared to adjacent midblock segments, reflecting shorter dwell times but higher near-miss intensity. In contrast, segments accumulate a significantly higher number of scenarios and vehicles due to sustained travel. For example, S7 (NE 19–17 St) records 308 northbound and 332 southbound scenarios involving more than 4000 vehicles, while S8 (NE 17–15 St) captures nearly 4400 vehicles in 608 scenarios.

Lane configurations vary between 2 and 3 lanes per direction, with average widths ranging from 3.1m (S7) to 3.6m (S6), indicating subtle but important differences in cross-sectional design. Driveway and minor intersection density also differs across the corridor: segments such as S3 and S4 contain four access points, while others like S5 and S6 have few or none, creating heterogeneous exposure to side-entry near-misses. Median type alternates between raised

Table 2
Profile of study locations along Biscayne Boulevard

ID	Location	Direction	Scenarios	Unique vehicles	Lane no	Lane width (m)	Driveway/Minor intersection	Median type
<i>Segment</i>								
S1	(NE 36–33 St)	NB / SB	131 / 111	1706 / 813	3 / 3	3.5	3	Raised
S2	(NE 33–29 St)	NB / SB	151 / 155	1532 / 1148	3 / 3	3.64	3	Raised
S3	(NE 29–26 St)	NB / SB	191 / 186	1721 / 1295	3 / 3	3.36	4	Flush paved
S4	(NE 26–22 St)	NB / SB	176 / 199	1542 / 1581	3 / 3	3.51	4	Flush paved
S5	(NE 22–21 St)	NB / SB	127 / 123	705 / 643	3 / 2	3.3	No	Flush paved
S6	(NE 21–19 St)	NB / SB	235 / 245	1588 / 1861	3 / 3	3.62	1	Flush paved
S7	(NE 19–17 St)	NB / SB	308 / 332	1704 / 2410	2 / 2	3.12	1	Flush paved
S8	(NE 17–15 St)	NB / SB	294 / 314	1955 / 2406	3 / 3	3.57	2	Flush paved
S9	(NE 15–13 St)	NB / SB	232 / 216	1565 / 1217	3 / 2	3.43	1	Flush paved
<i>Intersection</i>								
I1	NE 36 St	–	97	743	–	–	–	–
I2	NE 33 St	–	47	220	–	–	–	–
I3	NE 29 St	–	132	699	–	–	–	–
I4	NE 26 St	–	96	568	–	–	–	–
I5	NE 22 St	–	106	640	–	–	–	–
I6	NE 21 St	–	134	647	–	–	–	–
I7	NE 19 St	–	214	1332	–	–	–	–
I8	NE 17 St	–	205	1328	–	–	–	–
I9	NE 15 St	–	252	1332	–	–	–	–
I10	NE 13 St	–	232	1139	–	–	–	–

(e.g., S1–S2) and flush paved (e.g., S3–S9), influencing turning maneuvers and midblock encroachments. Overall, the table highlights that intersections serve as near-miss-prone nodes with concentrated but lower-volume interactions, whereas segments provide richer samples of continuous traffic flow, characterized by greater geometric variability.

Building on the spatial segmentation and detailed subregion profiles outlined above, the next step involves quantifying dynamic safety conditions using the proposed 2D-TTC framework (Algorithm 1). For each block, extreme near-miss events were identified by forward simulating vehicle trajectories under the geometric and traffic conditions described in Table 2. Both V–V and V–I interactions were modeled to reflect the heterogeneous near-miss environments of intersections and segments. Trajectories were projected over a 3s horizon, and spatial overlaps with surrounding traffic or roadway boundaries were detected as potential near-miss events. Representative outcomes from this process are shown in Fig. 6, illustrating the spatial dynamics of predicted V–V and V–I near-misses within the Miami study corridor. These event visualizations provide the empirical basis for block-level 2D-TTC extraction across the 10 intersections (I1–I10), enabling localized evaluation of crash-prone conditions.

Descriptive statistics of intersection-level V–V and V–I near-misses are summarized in Table 3. The continuous indicators include 2D-TTC, relative speed, acceleration, distance, jerk, and angular deviations (heading and steering), along with vehicle dimensions and exposure (volume). On average, 2D-TTC values for both near-miss types range between 1.3 and 1.6 s, with extreme cases falling below 0.1 s, reflecting highly critical near-miss conditions. V–I near-misses are associated with higher relative speeds and tighter distance gaps, indicating more abrupt encroachment against roadway boundaries. Conversely, V–V near-misses exhibit larger heading and steering deviations, along with higher jerk variability, suggesting unstable maneuvers such as sudden turns or evasive swerves. The categorical distribution of near-misses further illustrates key behavioral differences. Nearly three-quarters (72%) of V–V events occurred during through movements, with fewer during left (26%) or right (9%) turns. In contrast, V–I near-misses were almost entirely turning-related, with 46% occurring in left turns and 54% in right turns, and none during through movements. This pattern highlights that infrastructure-related near-misses typically occur during lateral maneuvers at intersections, where vehicles cross lane boundaries or encroach on curbs and medians.

Beyond intersections, the analysis was extended to directional roadway segments (S1–S9) using the same 2D-TTC framework (See Fig. 7). Table 4 summarizes descriptive statistics of both V–V and V–I near misses at the segment level. For V–V near-misses, average TTC values were longer (1.83 s) than those observed at intersections, suggesting greater temporal headway between vehicles in segment settings. However, the extreme minima (0.11 s) and high maximum relative speeds (up to 33.9 m/s) highlight the presence of aggressive overtaking and high-speed convergence. Relative distances also exhibited a much broader range (up to 141.5 m), indicating that near-misses often arise in more dispersed longitudinal interactions rather than tightly constrained intersection maneuvers.

For V–I near-misses, the mean TTC was shorter (1.27s), with relative speeds peaking at 28.1 m/s, underscoring the abrupt nature of vehicle–boundary encounters. Compared with intersections, segment-based V–I near-misses involved

Table 3
Summary statistics for V–V and V–I near-misses at Intersection

Metric	V–V				V–I			
	Avg	Min	Max	Std	Avg	Min	Max	Std
Continuous variables								
TTC	1.617	0.11	2.99	0.863	1.304	0.10	2.99	0.889
Relative speed	5.257	0.00	23.724	4.446	8.753	0.00	22.276	4.035
Relative acc/dec	-0.535	-13.706	10.343	2.227	0.161	-5.925	13.199	0.702
Relative distance	11.673	2.419	46.857	6.844	1.520	0.60	3.80	1.110
Jerk	-5.550	-13.609	9.315	2.652	-7.900	-10.800	2.800	14.700
Heading difference	1.077	0.00	6.251	1.410	-0.045	-3.138	3.141	1.647
Steering difference	0.409	0.00	3.142	0.666	-0.006	-1.571	1.571	0.130
Volume	13.462	2.00	31.00	5.969	10.461	1.00	31.00	5.392
Vehicle length	4.78	3.18	6.92	0.49	5.1	3.95	12.65	1.30
Vehicle width	2.22	1.76	3.16	0.30	2.04	1.36	3.08	0.23
Categorical variable: Near-miss location (Proportion %)								
Through	72.29			0.00				
Left Turn	25.99			46.08				
Right Turn	8.90			53.92				

longer approach distances but also showed greater instability in jerk and heading, reflecting frequent lateral drifts toward lane edges or curbs. These events often occurred near driveways and minor access points, where vehicles deviated from their intended path, creating encroachment risks. The categorical breakdown reinforces these patterns. For V–V events, nearly 59% of near-misses were associated with through movements, while about 32% and 10% were linked to right and left turns, respectively. In contrast, V–I near-misses were dominated by turning maneuvers, with more than half (53.9%) linked to right turns and 46% to left turns, and no near-misses detected during through movements. This distribution highlights the heightened role of lateral maneuvers in producing infrastructure-related risks. Furthermore, median type also influenced outcomes: 76% of V–V near-misses and 86% of V–I near-misses occurred along undivided sections, underscoring the vulnerability of open medians and flush-paved designs in segment environments.

Taken together, these segment-level findings reveal that while intersections are hotspots for tightly constrained V–V near-misses, segments carry distinctive risks tied to high-speed encounters and infrastructure encroachments. The observed distributions underscore the importance of treating intersections and segments as functionally distinct safety domains when modeling near-miss dynamics and designing targeted countermeasures.

After identifying and compiling the BM near-miss events for each observation unit (segments and intersections), the frequencies of extreme V–V and V–I events were systematically aggregated and visualized in Fig. 8. This plot illustrates the spatial distribution of extreme near-miss frequencies across 28 locations, comprising 10 intersections and 18 segments, organized into intersection zones, primary-direction segments, and opposite-direction segments. This spatial aggregation confirms the integrity of the BM dataset and provides the foundation for modeling. The study extends prior approaches by incorporating both V–V and V–I near misses into the HBSGRP–UGEV framework, explicitly integrating roadway geometry and infrastructure features alongside vehicle dynamics. Prior research has emphasized the role of vehicle kinematics in crash risk (Desai et al., 2021; Jun et al., 2007; Tak et al., 2015); here, additional geometric covariates, such as lane configuration and boundary proximity, are introduced. For example, high steering angles, often indicating abrupt lateral maneuvers—were included as predictors, given their link to boundary incursions and sudden evasive actions that may elevate near-miss risk (Gilbert et al., 2021). Fig. 8 highlights several notable spatial patterns. Opposite-direction segments (S82, S72, S62) exhibited the highest V–I frequencies, suggesting greater lateral variability and exposure to curb or median near-misses. Primary-direction segments (S11, S21, S81) showed elevated V–V near-miss frequencies, consistent with midblock environments dominated by longitudinal interactions such as close-following, lane changes, or overtaking. Among intersections, I7, I8, and I9 emerged as critical hotspots,

Table 4
Summary statistics for V–V and V–I near-misses at segments

Metric	V–V				V–I			
	Avg	Min	Max	Std	Avg	Min	Max	Std
Continuous variables								
TTC	1.829	0.11	2.99	0.805	1.272	0.10	2.99	0.912
Relative speed	4.513	0.00	33.909	4.278	10.262	0.000	28.067	4.212
Relative acc/dec	-0.871	-23.014	18.336	3.139	0.164	-14.067	23.343	1.400
Relative distance	15.361	1.931	141.548	12.773	1.720	0.32	6.56	1.02
Jerk	-7.121	-17.502	8.423	1.552	-5.70	-12.72	3.556	4.77
Heading difference	0.368	0.000	6.256	0.990	-0.032	-3.102	3.138	1.586
Steering difference	0.577	0.000	3.142	0.756	-0.001	-1.571	1.571	0.167
Volume	16.801	1.000	65.000	11.009	12.816	1.000	65.000	7.906
Vehicle Length	4.74	3.0	7.85	1.11	4.79	2.95	8.65	0.87
Vehicle width	2.12	1.36	3.08	0.23	2.22	1.76	4	0.18
Lane number	2.73	2	4	0.578	2.51	2.0	4.0	0.52
Lane width	3.28	2.99	3.96	0.14	3.27	2.99	3.96	0.141
Driveway intensity	0.009	0.000	0.015	0.005	0.009	0.000	0.015	0.005
Categorical variable: (Proportion %)								
Collision location	Through		58.55			0.00		
	Left Turn		9.52			46.08		
	Right Turn		31.93			53.92		
Median type	Divided		23.60			13.98		
	Undivided		76.4			86.02		

with elevated frequencies of both near-miss types. This dual concentration reflects the operational complexity of intersections, where near-missing maneuvers, pedestrian flows, and signal control interact to amplify crash potential.

The distribution and magnitude of near-miss counts across all locations validate the effectiveness of the BM approach in capturing rare but safety-critical events. Specifically, nearly all study sites meet or exceed the recommended minimum threshold of 30 BM events for reliable GEV-based inference (Zheng et al., 2014), with the exception of intersection I2. This ensures that the dataset is statistically robust for subsequent HBSGRP–UGEV analysis. The spatial heterogeneity revealed in Fig. 8 further underscores the need to incorporate direction-specific geometric and behavioral covariates within the modeling framework. These results provide compelling justification for developing localized, high-resolution safety models that integrate both roadway configuration and observed vehicle dynamics, thereby enabling precise and context-sensitive real-time risk assessments in complex urban environments.

5. Modeling estimation result

This study develops a series of Bayesian hierarchical UGEV models to estimate COR from extreme 2D-TTC near-miss events observed along Biscayne Boulevard in Miami. Extreme near-misses are identified using the BM approach, wherein the minimum 2D-TTC within each temporal block is treated as the most critical interaction. The theoretical foundations and implementation of this sampling methodology are detailed in prior research (2025b). Each V–V and V–I interaction is treated as an independent block. Because extreme events are sparse at individual sites, direct location-specific estimation can yield unstable posteriors with wide uncertainty intervals. To address this, a grouping strategy was adopted, pooling samples across functionally similar sites (intersections, segments) while still preserving local heterogeneity. This clustering approach improves estimation stability and aligns with prior network-level applications of UGEV models in traffic safety (Zheng et al., 2014; Fu and Sayed, 2021c).

The primary analytical framework is the HBSGRP–UGEV model, while a simpler fixed-effect hierarchical model (HBSFP) was estimated as a benchmark. Accordingly, two models were developed for each near-miss type: (1) HBSFP and (2) HBSGRP. The grouped random parameter specification allows selected coefficients to vary across spatial clusters, thereby capturing latent differences linked to roadway geometry and interaction dynamics. Model performance

was evaluated using the DIC (Spiegelhalter et al., 2002; El-Basyouny and Sayed, 2012b,a), where lower values indicate stronger predictive performance (Zheng et al., 2019).

Estimation was conducted using MultiBUGS, a parallelized extension of OpenBUGS tailored for high-dimensional Bayesian inference. Its support for block updating and parallel execution makes it well-suited for capturing spatial dependence, random effects, and extreme value behavior within complex data structures. Parameters were estimated by Markov Chain Monte Carlo (MCMC) simulation, two parallel MCMC chains of 50000 iterations were run, with the first 20000 discarded as burn-in and the remaining 30000 retained for posterior inference. Convergence was verified both visually (trace plots) and quantitatively (Brooks–Gelman–Rubin diagnostic), with all monitored parameters achieving BGR values below 1.1, indicating satisfactory convergence (Gelman and Rubin, 1992; Brooks and Gelman, 1998; El-Basyouny and Sayed, 2009). This estimation procedure yielded robust posterior summaries of means, standard deviations, and 95% credible intervals, even under correlation structures induced by spatial clustering and random effects.

The study incorporated a comprehensive set of covariates into the location (μ) and scale (σ) parameters of the non-stationary UGEV distribution to reflect contextual and behavioral variability in COR. For both V–V and V–I interactions, dynamic covariates included relative speed, distance, acceleration, deceleration, headway difference, steering angle difference, jerk and traffic volume, factors capturing key dimensions of vehicle dynamics and near-miss severity. Geometric and infrastructure related covariates were also included: lane number, lane width, driveway intensity, median type, and lane position for segment models; and a categorical indicator of turning movement for intersection models.

All covariates were specified in both μ and σ components, enabling the models to capture variation in both the central tendency and dispersion of extreme 2D-TTC. In contrast, the shape parameter (ξ) was held constant across all locations. This choice is deliberate: ξ governs tail heaviness in the UGEV distribution but is notoriously difficult to estimate from sparse BM samples. Allowing ξ to vary with covariates often induces instability and overfitting (Coles et al., 2001; Cooley et al., 2006). Fixing ξ improves convergence and yields more interpretable posterior distributions.

5.1. Posterior results and model performance

Tables 5 through 8 report the posterior summaries for both HBSFP and HBSGRP models, estimated separately for V–V and V–I near-misses at intersections and segments. Across all cases, the HBSGRP specification consistently outperformed the HBSFP baseline, confirming its ability to capture unobserved heterogeneity and location-level variability. The DIC values for the HBSGRP models were 508.9 (V–V) and 3179.6 (V–I) at intersections, and 4189.0 (V–V) and 6550.0 (V–I) at segments. These correspond to relative reductions in DIC of 3.41% and 0.54% at intersections, and 7.49% and 3.11% at segments, compared with their HBSFP counterparts. Such reductions exceed the widely accepted threshold of five DIC units, indicating statistically meaningful improvements in fit (El-Basyouny and Sayed, 2012b,a). To further assess model robustness, WAIC and LOOIC were also computed. Both measures produced rankings consistent with DIC, reinforcing the superior performance of the HBSGRP structure. By allowing selected coefficients to vary across spatial groups, the HBSGRP models capture latent heterogeneity in both the central tendency and dispersion of near-miss severity, which fixed-effect structures fail to represent. Collectively, these results demonstrate that grouped random parameter models provide a more flexible and accurate framework for modeling COR dynamics in complex urban traffic environments.

5.1.1. Intersection-level

The intersection-level HBSGRP–UGEV model was designed to capture the heterogeneity of extreme 2D-TTC distributions arising from V–V interactions at signalized locations. In the model specification stage, several covariates were tested as random effects; however, most roadway geometry variables exhibited negligible variation across sites and did not improve posterior fit. To maintain parsimony and interpretability, random effects were therefore restricted to the intercept and two dynamic covariates (relative speed and relative distance), while other vehicle dynamics and geometric features were retained as fixed effects, following recommendations from (Anis et al., 2025a). This choice reflects theoretical expectations: vehicle dynamics are highly variable across intersections depending on signal phasing, approach alignment, and driver behavior, whereas roadway structure tends to exert a more stable influence. The resulting specification captures both site-specific dynamics and broader geometric constraints, group-specific random effects illustrated in Fig. 9 with posterior summaries reported in Table 5.

The fixed-parameter benchmark (HBSFP) provides a baseline against which the grouped random specification can be compared. Consistent reductions in DIC, WAIC, and LOOIC confirm the superior fit of the HBSGRP model,

Table 5
Posterior estimates for V-V near misses at intersections

Model Parameters	Hyperparameter	Covariate	HBSFP			HBSGRP		
			Mean	SD ^a	95% CRI ^b	Mean	SD ^a	95% CRI ^b
<i>Location Parameter ($\mu_{k,i}$)</i>								
$\beta_{\mu,0}$	Fixed	Intercept	-1.870	0.039	[-1.917, -1.811] [†]	-	-	-
$\beta_{\mu,0,k}$	Random	Intercept	-	-	-	-1.893	0.186	[-2.309, -1.572] [†]
$\gamma_{\mu,1,k}$	Random	Relative speed	-	-	-	0.745	0.181	[0.393, 1.134] [†]
$\gamma_{\mu,2,k}$	Random	Relative distance	-	-	-	-0.491	0.157	[-0.819, -0.280] [†]
$\beta_{\mu,1}$	Fixed	Relative speed	0.639	0.050	[0.246, 0.739] [†]	-	-	-
$\beta_{\mu,2}$	Fixed	Relative acceleration	1.064	0.074	[0.126, 2.018] [†]	-0.155	0.032	[-0.221, -0.093] [†]
$\beta_{\mu,3}$	Fixed	Relative deceleration	-0.013	0.037	[-0.088, 0.059]	0.140	0.063	[0.004, 0.238] [†]
$\beta_{\mu,4}$	Fixed	Relative distance	-0.442	0.036	[-0.505, -0.418] [†]	-	-	-
$\beta_{\mu,5}$	Fixed	Jerk	-0.012	0.006	[-0.021, -0.002] [†]	-0.027	0.015	[-0.046, -0.006] [†]
$\beta_{\mu,6}$	Fixed	Heading difference	0.024	0.026	[-0.029, 0.072]	0.028	0.039	[-0.052, 0.097]
$\beta_{\mu,7}$	Fixed	Steering difference	-0.004	0.049	[-0.096, 0.092]	0.059	0.026	[0.003, 0.107] [†]
$\beta_{\mu,8}$	Fixed	Volume	-0.003	0.005	[-0.012, 0.006]	-0.018	0.035	[-0.085, 0.051]
$\beta_{\mu,9}$	Fixed	Turn movement (Left =1, else=0)	0.086	0.026	[-0.102, 0.242]	0.073	0.011	[0.042, 0.205] [†]
<i>Scale Parameter ($\log \sigma_{k,i}$)</i>								
$\beta_{\sigma,0}$	Fixed	Intercept	-0.571	0.058	[-0.680, -0.455] [†]	-	-	-
$\beta_{\sigma,0,k}$	Random	Intercept	-	-	-	-0.599	0.311	[-1.240, -0.056] [†]
$\gamma_{\sigma,1,k}$	Random	Relative speed	-	-	-	-0.265	0.254	[-0.810, -0.043] [†]
$\gamma_{\sigma,2,k}$	Random	Relative distance	-	-	-	-0.653	0.297	[-1.121, -0.033] [†]
$\beta_{\sigma,1}$	Fixed	Relative speed	0.012	0.084	[-0.139, 0.183]	-	-	-
$\beta_{\sigma,2}$	Fixed	Relative acceleration	-1.686	0.865	[-3.066, -0.627] [†]	-0.226	0.066	[-0.360, -0.108] [†]
$\beta_{\sigma,3}$	Fixed	Relative deceleration	-0.218	0.051	[-0.321, -0.120] [†]	-0.253	0.053	[-0.356, -0.151] [†]
$\beta_{\sigma,4}$	Fixed	Relative distance	-0.062	0.008	[-0.078, -0.046] [†]	-	-	-
$\beta_{\sigma,5}$	Fixed	Jerk	0.019	0.009	[0.005, 0.030] [†]	0.012	0.003	[0.007, 0.018] [†]
$\beta_{\sigma,6}$	Fixed	Heading difference	-0.063	0.071	[-0.212, 0.060]	-0.055	0.014	[-0.133, -0.026] [†]
$\beta_{\sigma,7}$	Fixed	Steering difference	0.063	0.065	[-0.061, 0.191]	-0.053	0.040	[-0.117, -0.011] [†]
$\beta_{\sigma,8}$	Fixed	Volume	-0.001	0.007	[-0.015, 0.013]	-0.004	0.044	[-0.090, 0.084]
$\beta_{\sigma,9}$	Fixed	Turn movement(Left =1, else=0)	0.042	0.120	[-0.183, 0.285]	0.217	0.123	[0.025, 0.471] [†]
<i>Shape Parameter ($\xi_{k,i}$)</i>								
$\beta_{\xi,0}$	Fixed	Intercept	-0.305	0.051	[-0.413, -0.208] [†]	-	-	-
$\beta_{\xi,0,k}$	Random	Intercept	-	-	-	-0.684	0.253	[-1.309, -0.314] [†]
<i>Model Fit</i>								
DIC			526.9			508.9		
WAIC			539.4			521.5		
LOOIC			540.1			522.3		

HBSFP Hierarchical Bayesian Spatial Fixed Parameter
HBSGRP Hierarchical Bayesian Spatial Grouped Random Parameter

^a Standard deviation

^b 95% Bayesian credible interval

- Covariate not included in the model

[†] Indicates statistical significance at the 95% level (interval excludes 0)

underscoring the explanatory value of allowing relative speed and spacing effects to vary across intersection clusters. The direction and magnitude of these coefficients provide valuable insights into the mechanisms underlying COR. The random-parameter specification highlights the spatially varying influence of relative speed and relative distance on both the location and scale components of the HBSGRP distribution. For μ , relative speed shows a positive effect across intersections, indicating that larger speed differentials between interacting vehicles lead to sharply reduced 2D-TTC values and more severe near-miss conditions. In contrast, relative distance is negatively associated with μ , meaning that shorter headways systematically increase near-miss severity by limiting the buffer available for evasive action. For σ , both covariates are associated with reduced variability in near-miss severity. Relative speed has a negative coefficient, suggesting that high-speed interactions produce consistently critical outcomes, dangerous but less variable, because drivers have little opportunity to recover through braking or swerving. Similarly, relative distance exerts a negative effect on σ , reflecting that short headways yield uniformly critical near-miss with little dispersion in outcomes. Together, these results confirm the physical intuition that speed amplifies severity while distance compresses

variability, producing deterministic near miss outcomes under constrained conditions. Fig. 9 further illustrate this spatial heterogeneity across intersection, while most locations show consistent trends, the I2 site exhibits unusually wide CI for the μ effects and CI exceed zero for the σ , across intercept, relative speed, and relative distance. This instability is directly attributable to I2's small BM sample size, which weakens posterior precision and introduces greater uncertainty in estimated group-level effects. Despite this, the overall pattern across intersections remains robust: relative speed consistently intensifies near-miss severity, while shorter distances exacerbate risk and constrain outcome variability.

Beyond the random effects, several covariates were modeled as fixed parameters due to their relatively stable contributions across intersections. Their interpretation reveals distinct roles of longitudinal dynamics, lateral control, maneuver type, and exposure effects in shaping near-miss severity and variability. Table 5 indicate that relative acceleration shows a significant negative effect on both the location and scale parameters. This suggests that acceleration is generally associated with smoother and less variable near-miss, consistent with situations where vehicles accelerate out of a green phase or clear an intersection without abrupt interaction. By contrast, relative deceleration exerts a positive effect on severity (μ) but a negative effect on variability (σ). This indicates that abrupt braking sharply intensifies near-misses but also produces more uniform outcomes, reflecting the deterministic nature of emergency deceleration in high-risk encounters. Jerk, which captures the rate of change in acceleration, has the opposite pattern: a negative effect on μ but a positive effect on σ . Although jerk slightly reduces average near-miss severity (perhaps due to hesitation or driver corrections), it simultaneously increases unpredictability in outcomes, highlighting the unstable nature of rapid throttle/brake oscillations.

Lateral vehicle dynamics also contribute meaningfully to near-miss risk estimation. Steering difference emerges as a significant contributor in the HBSGRP specification, showing a positive association with μ and a negative association with σ . This suggests that abrupt steering maneuvers intensify near-miss severity but lead to more consistent outcomes within constrained intersection geometries. Heading difference also shows a significant positively association with μ and a negatively with σ . Indicating that even small misalignments in trajectory lead to predictable patterns of near-miss outcomes, consistent with the rigid geometry of signalized approaches.

The categorical indicator for left-turn movements is significant and has a positive effect on both μ and σ . This aligns with the well-documented complexity of left-turn phases, which involve interactions with opposing through traffic and diverse driver decision strategies. The result suggests that left turns not only elevate near-miss severity but also introduce greater variability in outcomes, reflecting the wide range of intersection designs and driver behaviors under turning conditions. Traffic volume is statistically insignificant in both μ and σ . Nonetheless, it was retained in the model to ensure conceptual completeness, since it represents exposure. The lack of effect implies that short-duration 2D-TTC near-miss events are governed more by instantaneous vehicle interactions than by aggregate traffic demand.

Finally, the estimated shape parameter (ξ) is negative and significant across all intersections (Fig. 9g), indicating a bounded upper tail of the UGEV distribution. This supports the Weibull domain as the appropriate tail form for modeling extreme near-misses in signalized urban settings. Importantly, group-level variability in ξ suggests that intersection design and control strategies influence not only the frequency but also the extremal nature of near-miss outcomes.

The HBSGRP model for V-I near-misses specifies the intercept as a random parameter in both the location and scale components, capturing baseline heterogeneity in near-miss severity and variability across intersections. Relative speed (location) and relative distance (scale) were also treated as random effects (Fig. 10), though their 95% CI overlapped zero. They were retained on theoretical grounds, given their inclusion improve overall metrics. All other covariates were modeled as fixed effects, representing more stable behavioral and geometric influences. Fit statistics (Table 6) show modest but consistent improvements in DIC, WAIC, and LOOIC over the HBSFP benchmark, suggesting that the grouped random parameter structure adds nuance but yields smaller performance gains compared to the V-V case.

In the location parameter, several interpretable effects emerge. Relative distance is strongly negative and significant, confirming that reduced clearance to the roadway edge sharply lowers 2D-TTC, elevating severity. Relative deceleration also carries a significant negative sign, which contrasts with its positive effect in V-V near-miss. This suggests that braking near infrastructure reflects proactive yielding or evasive action, thereby limiting severity rather than escalating it. Heading and steering differences are positive and significant, indicating that lateral deviations (e.g., turning toward or away from curbs) increase near-miss severity. Left-turn movement, however, shows a significant negative association, suggesting that left-turn trajectories may provide greater clearance to boundaries, reducing average severity compared to right turns. This finding requires careful interpretation, as it may partly reflect geometric factors such as wider turning radii or reduced pedestrian/boundary overlap in left-turn phasing. Relative speed, though included as a random effect,

Table 6
Posterior estimates for V-I near misses at intersections

Model Parameters	Hyperparameter	Covariate	HBSFP			HBSGRP		
			Mean	SD ^a	95% CRI ^b	Mean	SD ^a	95% CRI ^b
<i>Location Parameter ($\mu_{k,i}$)</i>								
$\beta_{\mu,0}$	Fixed	Intercept	-1.392	0.039	[-1.461, -1.299] [†]	-	-	-
$\beta_{\mu,0,k}$	Random	Intercept	-	-	-	-1.401	0.092	[-1.598, -1.236] [†]
$\gamma_{\mu,1,k}$	Random	Relative speed	-	-	-	0.025	0.020	[-0.012, 0.065]
$\beta_{\mu,1}$	Fixed	Relative speed	-0.012	0.022	[-0.054, 0.031]	-	-	-
$\beta_{\mu,2}$	Fixed	Relative acceleration	-0.020	0.023	[-0.067, 0.022]	-0.020	0.024	[-0.068, 0.029]
$\beta_{\mu,3}$	Fixed	Relative deceleration	-0.066	0.013	[-0.075, -0.055] [†]	-0.026	0.011	[-0.071, -0.009] [†]
$\beta_{\mu,4}$	Fixed	Relative distance	-0.357	0.035	[-0.427, -0.290] [†]	-0.359	0.026	[-0.405, -0.306] [†]
$\beta_{\mu,5}$	Fixed	Jerk	0.270	0.355	[-0.457, 0.556]	-0.021	0.005	[-0.026, 0.01]
$\beta_{\mu,6}$	Fixed	Heading difference	0.040	0.022	[0.005, 0.084] [†]	0.062	0.026	[0.010, 0.127] [†]
$\beta_{\mu,7}$	Fixed	Steering difference	0.009	0.018	[-0.027, 0.045]	0.038	0.022	[0.014, 0.074] [†]
$\beta_{\mu,8}$	Fixed	Volume	-0.017	0.021	[-0.061, 0.023]	-0.023	0.023	[-0.069, 0.027]
$\beta_{\mu,9}$	Fixed	Turn movement (Left =1, else=0)	-0.129	0.080	[-0.265, -0.061] [†]	-0.579	0.310	[-1.231, -0.220] [†]
<i>Scale Parameter ($\log \sigma_{k,i}$)</i>								
$\beta_{\sigma,0}$	Fixed	Intercept	-0.100	0.038	[-0.167, -0.009] [†]	-	-	-
$\beta_{\sigma,0,k}$	Random	Intercept	-	-	-	-0.197	0.098	[-0.374, -0.001] [†]
$\gamma_{\sigma,1,k}$	Random	Relative distance	-	-	-	0.042	0.034	[-0.028, 0.107]
$\beta_{\sigma,1}$	Fixed	Relative speed	0.036	0.019	[0.013, 0.063] [†]	0.040	0.019	[0.001, 0.076] [†]
$\beta_{\sigma,2}$	Fixed	Relative acceleration	0.012	0.015	[-0.015, 0.042]	0.046	0.011	[0.009, 0.084] [†]
$\beta_{\sigma,3}$	Fixed	Relative deceleration	-0.147	0.056	[-0.285, -0.027] ^{†g}	-0.177	0.056	[-0.289, -0.047] [†]
$\beta_{\sigma,4}$	Fixed	Relative distance	0.209	0.038	[0.140, 0.282] [†]	-	-	-
$\beta_{\sigma,5}$	Fixed	Jerk	0.611	0.133	[0.227, 0.886] [†]	0.109	0.033	[0.016, 0.156] [†]
$\beta_{\sigma,6}$	Fixed	Heading difference	-0.023	0.018	[-0.057, -0.004] [†]	-0.090	0.021	[-0.130, -0.049] [†]
$\beta_{\sigma,7}$	Fixed	Steering difference	-0.012	0.018	[-0.045, 0.023]	-0.024	0.020	[-0.062, -0.017] [†]
$\beta_{\sigma,8}$	Fixed	Volume	0.004	0.016	[-0.028, 0.034]	0.029	0.018	[0.003, 0.064] [†]
$\beta_{\sigma,9}$	Fixed	Turn movement (Left =1, else=0)	0.100	0.053	[0.019, 0.197] [†]	0.264	0.049	[0.163, 0.349] [†]
<i>Shape Parameter ($\xi_{k,i}$)</i>								
$\beta_{\xi,0}$	Fixed	Intercept	-0.677	0.042	[-0.749, -0.594] [†]	-	-	-
$\beta_{\xi,0,k}$	Random	Intercept	-	-	-	-0.680	0.096	[-0.876, -0.501] [†]
<i>Model Fit</i>								
DIC			3197			3179.6		
WAIC			3202			3194.4		
LOOIC			3212.87			3209.8		

HBSFP Hierarchical Bayesian Spatial Fixed Parameter

HBSGRP Hierarchical Bayesian Spatial Grouped Random Parameter

^a Standard deviation

^b 95% Bayesian credible interval

- Covariate not included in the model

[†] Indicates statistical significance at the 95% level (interval excludes 0)

is not significant in the pooled analysis, highlighting that V-I risks are less sensitive to speed differentials than V-V encounters.

The scale parameter results add further insight into variability. The negative random intercept suggests baseline differences across intersections, with some sites producing more predictable outcomes than others. Relative speed exhibits a positive and significant association with scale, implying that faster approaches to infrastructure yield greater variability in severity—contrasting with the V-V case, where speed reduced dispersion. This difference reflects the inherently diverse driver responses to boundary proximity: some brake aggressively, while others take wider trajectories or maintain speed. Relative acceleration is also positive and significant, reinforcing the idea that heterogeneous driver behavior during acceleration near boundaries widens outcome variability. In contrast, relative deceleration has a significant negative effect on scale, meaning that strong braking compresses the severity distribution into consistently critical outcomes. Jerk is similarly positive, confirming that abrupt longitudinal control amplifies variability. Lateral dynamics again exhibit distinct roles: heading and steering differences reduce variability, suggesting that once a driver commits to a lateral maneuver, outcomes become more predictable. Finally, left-turn movement increases variability

despite lowering average severity, consistent with heterogeneous geometric layouts and driver strategies in left-turn contexts.

The shape parameter remains negative and significant across intersections, supporting the Weibull domain for V–I near misses and confirming that these events have a bounded upper tail. This implies a physical or behavioral limit to how severe boundary near-misses can become, constrained by roadway geometry and driver response capacity. Spatial variation in the shape parameter underscores the role of intersection design and infrastructure placement in shaping the extremal properties of near-miss distributions. Overall, the intersection-level results suggest that V–I near-misses are driven more by clearance, braking behavior, and lateral maneuvers than by speed differentials. Unlike V–V near-misses, where high speeds produce deterministic severity, V–I near-misses are marked by greater variability, reflecting the complex interplay between infrastructure geometry, driver avoidance strategies, and intersection control.

5.2. Segment-level

The HBSGRP model for segment-level V–V near misses introduces random parameters within a hierarchical framework (Table 7). Allowing the intercept and three time-varying vehicle-based measures, relative speed, relative deceleration, and relative distance, to vary across segments (See Fig. 11). This specification acknowledges that longitudinal dynamics in uninterrupted midblock contexts are shaped not only by vehicle behavior but also by geometric features such as lane configuration, median presence, and driveway density. All remaining covariates, including relative acceleration, jerk, heading and steering differences, traffic volume, lane attributes, and access density, were modeled as fixed effects due to their comparatively stable influence across segments. The HBSGRP specification produces substantial improvements in model fit over the HBSFP baseline, confirming the value of partial pooling in capturing heterogeneity across the nine directional segments analyzed.

For the location parameter (μ), random effects highlight systematic heterogeneity across the nine directional segments. Relative speed exerts a significant positive effect, confirming that higher closing speeds consistently compress available 2D-TTC and elevate near-miss severity. However, the posterior distributions in Fig. 11 reveal that the magnitude of this effect varies substantially across segments. Segments with uninterrupted, high-speed flows (e.g., S11) show stronger effects, while others with denser access points (e.g., S6, S7 and S13) exhibit wider credible intervals. Relative deceleration also carries a negative sign, though with more overlap in its credible intervals across segments, suggesting that emergency braking may sometimes mitigate severity in smoother-flow environments, while in higher-speed segments it intensifies near-misses. Notably, in some lower-sample segments, credible intervals for the location intercept approach or cross zero, reflecting weaker estimation stability under sparse BM events. Relative distance displays a consistently negative effect across segments, meaning that shorter headways reliably reduce 2D-TTC, yet its posterior variation underscores differences in spacing behavior along divided versus undivided facilities.

Among the fixed effects, relative acceleration shows a significant negative coefficient in both models, implying that acceleration phases are systematically linked to higher near-miss severity on segments. This contrasts with intersection contexts, where acceleration often reflected flow resumption. Here, aggressive acceleration during overtaking or merging maneuvers reduces spacing and increases risk. Jerk is also negative, reinforcing the role of abrupt longitudinal control in producing critical outcomes. Lateral control indicators—heading and steering differences—show positive signs, suggesting that lateral adjustments modestly increase 2D-TTC where lane-changing flexibility exists. Driveway density exhibits a strong positive effect on μ , which may appear counterintuitive, but is likely explained by anticipatory driver caution in access-rich environments. Conversely, undivided medians sharply reduce μ , indicating that exposure to opposing flows creates consistently severe interactions.

For the scale parameter (σ), the random effects for relative speed, deceleration, and distance are all negative, showing that extreme dynamics compress outcome variability, leading to uniformly critical near misses. The plots confirm this: high-speed and short-spacing conditions cluster tightly around lower 2D-TTC values, with narrow posteriors in segments such as S12 and S15. In contrast, segments like S10 display wider CI for random scale effects, again reflecting limited BM sample sizes. Fixed effects add further nuance: jerk and heading difference increase scale, suggesting that volatile acceleration or lateral corrections introduce heterogeneity in outcomes, while lane number and lane width reduce scale, indicating that greater maneuvering space fosters more predictable near-misses. Driveway density increases dispersion, consistent with the variability introduced by frequent merging and crossing maneuvers. Median type again exerts a strong negative influence, reinforcing that the absence of raised medians compresses severity outcomes into consistently critical ranges.

Finally, the shape parameter (ξ) remains negative and significant across segment groups, confirming a bounded upper tail consistent with the Weibull domain. This indicates physical and behavioral limits to maximum 2D-TTC

values during critical segment near-misses, constrained by speed environment, geometry, and driver reaction times. Posterior variation in the shape intercept suggests that undivided segments experience steeper extremal limits, while divided facilities allow marginally greater spread in outcomes. Overall, the segment-level results highlight the primacy of longitudinal dynamics in shaping corridor risk, with acceleration, braking, and headway dominating near-miss severity, while roadway design elements such as medians, lane width, and access density govern both severity and variability. The superior fit of the HBSGRP model underscores the importance of capturing these segment-specific dynamics, as fixed-parameter structures fail to account for the spatially contingent influence of speed and spacing across midblock contexts.

The HBSGRP specification for segment-level V–I near-misses provides a detailed view of how longitudinal dynamics and roadway design influence the severity and variability of extreme 2D-TTC outcomes (Table 8, Fig. 12). In this model, the intercept and relative distance are treated as group-level random effects in both the location and scale components of the HBSGRP model, allowing for spatial heterogeneity in how spacing between interacting vehicles shapes COR across segments. All other predictors—including relative speed, acceleration, deceleration, jerk, heading difference, steering angle difference, traffic volume, lane attributes, driveway density, median type, and left-lane presence, are modeled as fixed effects, reflecting their expected stability across segment environments.

For the location parameter, shorter relative distances strongly reduce 2D-TTC values, confirming that closer spacing consistently produces more critical near-miss outcomes. The random effect for distance further indicates that influence varies by segment group, suggesting sensitivity to local geometric or operational conditions. Relative speed displays a notable divergence: while the fixed-parameter benchmark shows a negative coefficient, the grouped model produces a small but positive estimate, implying that in certain contexts, higher speeds are associated with marginally longer 2D-TTC values. This reversal highlights that segment-level heterogeneity in speed environments, such as free-flow arterials versus constrained multilane facilities, can fundamentally alter the role of speed in shaping severity. Relative acceleration emerges as a significant positive effect in the grouped specification, suggesting that acceleration phases along segments may often represent clearance or recovery maneuvers rather than heightened near-miss risk. In contrast, relative deceleration maintains a negative coefficient across both models, reflecting the reality that braking during close-following conditions is tied to critical reductions in 2D-TTC, likely triggered by sudden evasive actions.

Several geometric and operational features are also important for location. Heading and steering differences exhibit significant positive coefficients, indicating that lateral adjustments yield small gains in clearance and mitigate near-miss severity. Volume, lane number, and lane width also emerge as positive contributors in the HBSGRP specification, suggesting that higher-capacity, wider facilities afford drivers greater maneuvering space, leading to slightly larger 2D-TTC values. The effect of driveway density, however, is particularly striking: while insignificant in the fixed-parameter model, the grouped specification produces a large negative estimate with a wide CI. This instability suggests that driveway effects are highly localized—segments with dense access points may concentrate more severe near-miss outcomes, but the data are sparse and sensitive to segment-specific characteristics. Median type is also significant, with undivided facilities consistently producing lower 2D-TTC values, reflecting heightened exposure to opposing traffic flows. The left-lane variable shows a sign reversal, with the fixed model suggesting higher severity in interior lanes and the grouped model indicating greater severity in outer lanes. This again illustrates heterogeneity across segment groups, where the positional context of a lane relative to roadside boundaries and merging activity shifts the locus of risk.

The scale parameter provides complementary insights into the dispersion of near-miss severity. The random effect for relative distance is positive, showing that tighter spacing increases not only severity but also variability in outcomes, as different drivers adopt divergent strategies under minimal headway conditions. Relative speed also has a positive association with scale, indicating that higher speeds amplify heterogeneity in outcomes across V–I interactions, unlike in V–V segment near-misses, where speed reduces dispersion. Acceleration, by contrast, has a negative coefficient in the grouped model, suggesting that acceleration phases yield more predictable outcomes, consistent with smoother-flow recovery dynamics. Relative deceleration also reduces variability, implying that braking in near-crash contexts converges toward uniformly critical outcomes.

Geometric attributes reveal nuanced effects on variability. Lane width exerts a positive effect, suggesting that while wider lanes modestly reduce average severity, they also introduce greater variability in outcomes by enabling diverse driver responses. The undivided median type strongly increases scale, underscoring that undivided facilities not only heighten the average risk but also broaden the range of severity outcomes, likely due to variation in driver avoidance maneuvers. The left-lane effect is positive in scale, indicating that severity outcomes in these lanes are more heterogeneous, perhaps reflecting the diversity of driver strategies in navigating outer versus inner lanes. Driveway

density, although statistically unstable, shows a wide and imprecise effect that suggests variability is strongly contingent on site-specific access management patterns.

The shape parameter remains negative and significant across both specifications, confirming that the upper tail of the 2D-TTC distribution is bounded. This supports the Weibull characterization of extremes, implying that even in segment-level V-I interactions, physical and behavioral limits constrain how severe the most critical near-miss events can be. Variation in shape across segment groups highlights the role of local geometry, access density, and operational features in shaping the extremal properties of near-miss distributions.

Together, the segment-level analyses of V-V and V-I near misses underscore that roadway geometry and vehicle dynamics interact to shape both the severity and variability of extreme near-misses. For V-V events, relative speed and distance dominate as key random effects, with speed consistently amplifying severity and distance compressing variability, reflecting deterministic outcomes under close-following conditions. For V-I events, however, the role of speed is more heterogeneous—sometimes protective, sometimes risk-enhancing—depending on the segment context. Access-related variables, particularly driveway density and median type, emerge as critical for V-I outcomes, underscoring the importance of access management and median design in shaping roadside safety. In both near-miss types, the negative and significant shape parameter indicates bounded extremes, reinforcing the physical and behavioral limits to crash risk escalation.

6. Model validation

The dataset for the study corridor provides precise geolocation for each extreme near-miss event and readily available annual corridor-level observed crashes. The dataset for the study corridor provides precise geolocation for each extreme near-miss event from Eqn. 32. To address this limitation, validation was conducted as an event-level case-control approach, designed to assess whether the model assigns higher predicted probabilities to more severe near-miss events. Posterior exceedance probabilities were computed from Eqn. 30 for severity thresholds ranging from -0.1 to -0.9 seconds, and these probabilities were then used to evaluate classification performance using the area under the receiver operating characteristic curve (ROC-AUC). This metric is particularly well-suited to rare-event prediction because it is independent of a specific threshold.

ROC curves were generated for the four HBSGRP-UGEV variants, covering both V-V, V-I interactions at segment and intersection levels. The results (Figure 13) reveal clear distinctions across near-miss types and roadway contexts. The segment-level V-V model consistently achieved the highest accuracy, with mean AUC values of about 0.89 and very little variation across thresholds. This indicates stable and robust predictive performance, reflecting the ability of grouped random parameters to capture high-speed longitudinal near-miss dynamics along uninterrupted midblock segments. The V-I model at the segment level achieved slightly lower accuracy, averaging around 0.79, and exhibited moderate sensitivity to the choice of severity threshold, a finding consistent with the greater variability in driver responses when vehicles approach roadside boundaries. At intersections, the V-V model demonstrated moderately strong predictive accuracy, with an average AUC of nearly 0.82 and relatively low volatility across thresholds. This indicates that grouped speed and spacing dynamics remain reliable even under more complex signalized and turning conditions. By contrast, the intersection-level V-I model performed weakest, averaging an AUC of approximately 0.75 and showing large fluctuations across thresholds, which reflects the complexity of boundary-related near-misses in intersections where turning trajectories, curb proximity, traffic signals, and pedestrian activity all interact.

Taken together, these findings confirm that the HBSGRP-UGEV framework provides strong and reliable performance for V-V interactions, particularly in segment environments, while predictions for V-I interactions are more sensitive to threshold selection and local variability. This suggests that segment-level V-V estimates are the most operationally reliable for proactive safety monitoring, whereas intersection-level V-I near-misses may require further refinement. Incorporating more detailed information on curb geometry, pedestrian exposure, and high-resolution vehicle-infrastructure proximity measures could improve stability and predictive accuracy in future applications.

7. Summary and conclusions

This study addresses the persistent challenge of accurately estimating short-term crash occurrence risk (COR) in complex, mixed urban traffic environments, where conventional surrogate safety models often overlook detailed vehicle geometry, roadway context, and site-specific behavioral variability. Existing approaches are limited by oversimplified near-miss representations, a predominant focus on vehicle-vehicle (V-V) interactions, and insufficient integration of

spatial heterogeneity in statistical modeling. To overcome these gaps, we propose a high-fidelity, geometry-aware, and statistically robust framework for real-time COR estimation that introduces a novel two-dimensional time-to-collision (2D-TTC) indicator. This metric accounts for vehicle dimensions, dynamic states, and precise geometric positioning, enabling accurate detection of extreme near-miss events from both V–V and vehicle–infrastructure (V–I) interactions.

Extreme events are translated into probabilistic risk estimates through a non-stationary Univariate Generalized Extreme Value (UGEV) framework implemented within a Hierarchical Bayesian Spatial Grouped Random Parameter (HBSGRP) structure. A corridor-based grouping strategy was employed to address event sparsity, pooling near-miss samples across intersections and directional segments while preserving local heterogeneity. Execution of the framework involved extracting high-resolution vehicle trajectories from the Argoverse-2 motion forecasting dataset, integrating them with HD maps and supplementary roadway information, and identifying near-miss events. The model incorporated both vehicle dynamics covariate (relative speed, acceleration, deceleration, jerk, heading difference, steering difference, and traffic volume) and geometric or operational covariates (lane number, lane width, driveway density, median type, turning movement, and vehicle lane position). Grouped random parameters were specified for temporally varying dynamics, relative speed, relative deceleration, and relative distance, to capture their context-dependent effects. For benchmarking, a baseline hierarchical Bayesian fixed-parameter (HBSFP) model was also estimated.

Results demonstrate that HBSGRP consistently outperformed the HBSFP across both intersections and segments, achieving lower DIC, WAIC, and LOOIC values and providing greater estimation stability. Relative speed emerged as the dominant predictor of near-miss severity in intersections, while relative distance was more influential for segment-level V–V events. Deceleration played a critical role in segment-level V–V near-miss, underscoring the importance of longitudinal control. Fixed covariates such as heading difference, steering difference, lane width, driveway density, and median type also showed significant effects, demonstrating the ability of the model to capture both dynamic behaviors and roadway design influences.

Validation results further confirmed model credibility. ROC–AUC analysis showed strong predictive performance, with V–V segment models achieving the highest accuracy ($AUC \approx 0.89$), followed by intersection V–V (≈ 0.82). V–I models performed reasonably well (segment ≈ 0.79 ; intersection ≈ 0.75) but displayed greater sensitivity to severity threshold choice. These findings highlight that while V–V interactions are modeled with high stability, V–I near-misses especially at intersections, remain more complex and variable.

Despite its contributions, the study has several limitations. First, potential bias may arise from the dependence on AV onboard sensors, which may affect traffic state accuracy and near-miss detection. Second, the 2D-TTC formulation, while tractable, simplifies nonlinear vehicle dynamics, which could understate risks in extreme evasive maneuvers. Third, the current framework does not explicitly model near-miss severity levels. Future research should extend the framework to multivariate UGEV models incorporating complementary surrogate measures such as post-collision velocity change (ΔV) and explicitly address vulnerable road user (VRU) near-misses. Broader validation across multiple cities, transferability calibration, and comparison with peaks-over-threshold (POT) GPD methods will further strengthen robustness and generalizability. As autonomous vehicle deployment increases, access to larger and richer trajectory datasets will enhance the statistical power of extreme value analysis and enable more nuanced safety assessments. In practice, the proposed HBSGRP–UGEV framework offers a scalable, data-driven tool for proactive safety monitoring at the corridor level. By enabling early identification of high-risk conditions and supporting real-time traffic management, it provides a pathway toward Vision Zero objectives, reducing fatalities and serious injuries while promoting safe, efficient, and equitable mobility in urban environments.

Acknowledgement: This research is funded by Federal Highway Administration (FHWA) Exploratory Advanced Research 693JJ323C000010. The results do not reflect FHWA’s opinions.

Disclaimer: The results presented in this document do not necessarily reflect those from the Federal Highway Administration.

Data availability: Data and code will be made available on reasonable request.

CRedit authorship contribution statement

Mohammad Anis: Conceptualization, Methodology, Writing – original draft, Software, Writing – review & editing. **Yang Zhou:** Conceptualization, Methodology, Writing – review & editing, Supervision. **Dominique Lord:** Conceptualization, Methodology, Writing – review & editing, Supervision.

References

- Ali, Y., Haque, M.M., Mannering, F., 2023a. Assessing traffic conflict/crash relationships with extreme value theory: Recent developments and future directions for connected and autonomous vehicle and highway safety research. *Analytic methods in accident research*, 100276.
- Ali, Y., Haque, M.M., Zheng, Z., 2022. An extreme value theory approach to estimate crash risk during mandatory lane-changing in a connected environment. *Analytic methods in accident research* 33, 100193.
- Ali, Y., Washington, S., Haque, M.M., 2023b. Estimating real-time crash risk at signalized intersections: A bayesian generalized extreme value approach. *Safety science* 164, 106181.
- Allen, B.L., Shin, B.T., Cooper, P.J., 1978. Analysis of traffic conflicts and collisions. Technical Report. New Astron.
- Alozi, A.R., Hussein, M., 2022. Evaluating the safety of autonomous vehicle–pedestrian interactions: An extreme value theory approach. *Analytic methods in accident research* 35, 100230.
- Anis, M., Geedipally, S.R., Lord, D., 2025a. Pedestrian crash causation analysis near bus stops: Insights from random parameters negative binomial–lindley model. *Accident Analysis & Prevention* 220, 108137.
- Anis, M., Li, S., Geedipally, S.R., Zhou, Y., Lord, D., 2025b. Real-time risk estimation for active road safety: Leveraging waymo av sensor data with hierarchical bayesian extreme value models. *Accident Analysis & Prevention* 211, 107880.
- Arun, A., Haque, M.M., Bhaskar, A., Washington, S., Sayed, T., 2021. A systematic mapping review of surrogate safety assessment using traffic conflict techniques. *Accident Analysis & Prevention* 153, 106016.
- Blincoe, L., Miller, T., Wang, J.S., Swedler, D., Coughlin, T., Lawrence, B., Guo, F., Klauer, S., Dingus, T., 2023. The economic and societal impact of motor vehicle crashes, 2019 (Revised). Technical Report DOT HS 813 403. National Highway Traffic Safety Administration.
- Brooks, S.P., Gelman, A., 1998. General methods for monitoring convergence of iterative simulations. *Journal of computational and graphical statistics* 7, 434–455.
- Caesar, H., Bankiti, V., Lang, A.H., Vora, S., Liong, V.E., Xu, Q., Krishnan, A., Pan, Y., Baldan, G., Beijbom, O., 2020. nuscenes: A multimodal dataset for autonomous driving, in: *Proceedings of the IEEE/CVF conference on computer vision and pattern recognition*, pp. 11621–11631.
- Cai, Q., Abdel-Aty, M., Lee, J., Wang, L., Wang, X., 2018. Developing a grouped random parameters multivariate spatial model to explore zonal effects for segment and intersection crash modeling. *Analytic methods in accident research* 19, 1–15.
- Chen, J., Jönsson, P., Tamura, M., Gu, Z., Matsushita, B., Eklundh, L., 2004. A simple method for reconstructing a high-quality ndvi time-series data set based on the savitzky–golay filter. *Remote sensing of Environment* 91, 332–344.
- Choi, J., Chin, H., Park, H., Kwon, D., Baek, D., Lee, S.H., 2024. Safe and efficient trajectory optimization for autonomous vehicles using b-spline with incremental path flattening. *IEEE Transactions on Intelligent Transportation Systems*.
- Coles, S., Bawa, J., Trenner, L., Dorazio, P., 2001. An introduction to statistical modeling of extreme values. volume 208. Springer.
- Cooley, D., Naveau, P., Pomelli, V., Rabatel, A., Grancher, D., 2006. A bayesian hierarchical extreme value model for lichenometry. *Environmetrics: The official journal of the International Environmetrics Society* 17, 555–574.
- Davis, G.A., Hordos, J., Xiong, H., Chatterjee, I., 2011. Outline for a causal model of traffic conflicts and crashes. *Accident Analysis & Prevention* 43, 1907–1919.
- Desai, J., Li, H., Mathew, J.K., Cheng, Y.T., Habib, A., Bullock, D.M., 2021. Correlating hard-braking activity with crash occurrences on interstate construction projects in indiana. *Journal of big data analytics in transportation* 3, 27–41.
- Eilers, P.H., Marx, B.D., 1996. Flexible smoothing with b-splines and penalties. *Statistical science* 11, 89–121.
- El-Basyouny, K., Sayed, T., 2009. Urban arterial accident prediction models with spatial effects. *Transportation research record* 2102, 27–33.
- El-Basyouny, K., Sayed, T., 2012a. Measuring direct and indirect treatment effects using safety performance intervention functions. *Safety science* 50, 1125–1132.
- El-Basyouny, K., Sayed, T., 2012b. Measuring safety treatment effects using full bayes non-linear safety performance intervention functions. *Accident Analysis & Prevention* 45, 152–163.
- Ettinger, S., Cheng, S., Caine, B., Liu, C., Zhao, H., Pradhan, S., Chai, Y., Sapp, B., Qi, C.R., Zhou, Y., et al., 2021. Large scale interactive motion forecasting for autonomous driving: The waymo open motion dataset, in: *Proceedings of the IEEE/CVF International Conference on Computer Vision*, pp. 9710–9719.
- Fu, C., Sayed, T., 2021a. Comparison of threshold determination methods for the deceleration rate to avoid a crash (drac)-based crash estimation. *Accident Analysis & Prevention* 153, 106051.
- Fu, C., Sayed, T., 2021b. Multivariate bayesian hierarchical gaussian copula modeling of the non-stationary traffic conflict extremes for crash estimation. *Analytic methods in accident research* 29, 100154.
- Fu, C., Sayed, T., 2021c. Random parameters bayesian hierarchical modeling of traffic conflict extremes for crash estimation. *Accident Analysis & Prevention* 157, 106159.
- Fu, C., Sayed, T., 2022a. Bayesian dynamic extreme value modeling for conflict-based real-time safety analysis. *Analytic methods in accident research* 34, 100204.
- Fu, C., Sayed, T., 2022b. Random-parameter bayesian hierarchical extreme value modeling approach with heterogeneity in means and variances for traffic conflict–based crash estimation. *Journal of transportation engineering, Part A: Systems* 148, 04022056.
- Fu, C., Sayed, T., 2023. Identification of adequate sample size for conflict-based crash risk evaluation: an investigation using bayesian hierarchical extreme value theory models. *Analytic methods in accident research* 39, 100281.

- Geiger, A., Lenz, P., Stiller, C., Urtasun, R., 2013. Vision meets robotics: The kitti dataset. *The international journal of robotics research* 32, 1231–1237.
- Gelman, A., Rubin, D.B., 1992. Inference from iterative simulation using multiple sequences. *Statistical science* 7, 457–472.
- Ghoul, T., Sayed, T., 2025. Cyclist safety assessment using autonomous vehicles. *Accident Analysis & Prevention* 212, 107923.
- Gilbert, A., Petrovic, D., Pickering, J.E., Warwick, K., 2021. Multi-attribute decision making on mitigating a collision of an autonomous vehicle on motorways. *Expert Systems with Applications* 171, 114581.
- Guo, Y., Essa, M., Sayed, T., Haque, M.M., Washington, S., 2019. A comparison between simulated and field-measured conflicts for safety assessment of signalized intersections in australia. *Transportation research part C: emerging technologies* 101, 96–110.
- Hayward, J., 1971. Near misses as a measure of safety at urban intersections. Pennsylvania Transportation and Traffic Safety Center.
- Houston, J., Zuidhof, G., Bergamini, L., Ye, Y., Chen, L., Jain, A., Omari, S., Igloukov, V., Ondruska, P., 2021. One thousand and one hours: Self-driving motion prediction dataset, in: *Conference on Robot Learning*, PMLR. pp. 409–418.
- Hussain, F., Li, Y., Arun, A., Haque, M.M., 2022. A hybrid modelling framework of machine learning and extreme value theory for crash risk estimation using traffic conflicts. *Analytic methods in accident research* 36, 100248.
- Islam, A.M., Shirazi, M., Lord, D., 2023. Grouped random parameters negative binomial-lindley for accounting unobserved heterogeneity in crash data with preponderant zero observations. *Analytic methods in accident research* 37, 100255.
- Islam, Z., Abdel-Aty, M., Cai, Q., Yuan, J., 2021. Crash data augmentation using variational autoencoder. *Accident Analysis & Prevention* 151, 105950.
- Jun, J., Ogle, J., Guensler, R., 2007. Relationships between crash involvement and temporal-spatial driving behavior activity patterns: use of data for vehicles with global positioning systems. *Transportation Research Record* 2019, 246–255.
- Kamel, A., Sayed, T., 2024. Transferability of real-time evt safety models: an investigation using autonomous vehicles data. *Transportmetrica A: Transport Science* , 1–26.
- Kamel, A., Sayed, T., Fu, C., 2023. Real-time safety analysis using autonomous vehicle data: a bayesian hierarchical extreme value model. *Transportmetrica B: Transport Dynamics* 11, 826–846.
- Kamel, A., Sayed, T., Kamel, M., 2024. Real-time combined safety-mobility assessment using self-driving vehicles collected data. *Accident Analysis & Prevention* 199, 107513.
- Kar, P., Venthuruthiyil, S.P., Chunchu, M., 2023. Non-stationary crash risk modelling of powered two-wheelers using extreme value analysis of surrogate crash events. *Accident Analysis & Prevention* 183, 106973.
- Kar, P., Venthuruthiyil, S.P., Chunchu, M., 2024. Crash risk estimation of heavy commercial vehicles on horizontal curves in mountainous terrain using proactive safety method. *Accident Analysis & Prevention* 199, 107521.
- Kesten, R., Usman, M., Houston, J., Pandya, T., Nadhamuni, K., Ferreira, A., Yuan, M., Low, B., Jain, A., Ondruska, P., Omari, S., Shah, S., Kulkarni, A., Kazakova, A., Tao, C., Platinsky, L., Jiang, W., Shet, V., 2019. Lyft level 5 av dataset 2019. <https://level5.lyft.com/dataset/>.
- Kumar, A., Mudgal, A., 2024. Risk assessment of rear-end crashes by incorporating vehicular heterogeneity into bayesian hierarchical extreme value models. *Transportmetrica B: Transport Dynamics* 12, 2323058.
- Lanzaro, G., Sayed, T., Fu, C., 2023. A comparison of pedestrian behavior in interactions with autonomous and human-driven vehicles: An extreme value theory approach. *Transportation research part F: traffic psychology and behaviour* 99, 1–18.
- Lee, J., Abdel-Aty, M., Cai, Q., 2017. Intersection crash prediction modeling with macro-level data from various geographic units. *Accident Analysis & Prevention* 102, 213–226.
- Li, P., Abdel-Aty, M., Yuan, J., 2020. Real-time crash risk prediction on arterials based on lstm-cnn. *Accident Analysis & Prevention* 135, 105371.
- Li, S., Anis, M., Lord, D., Zhang, H., Zhou, Y., Ye, X., 2024. Beyond 1d and oversimplified kinematics: A generic analytical framework for surrogate safety measures. *Accident Analysis & Prevention* 204, 107649.
- Lord, D., Mannering, F., 2010. The statistical analysis of crash-frequency data: A review and assessment of methodological alternatives. *Transportation research part A: policy and practice* 44, 291–305.
- Lord, D., Qin, X., Geedipally, S.R., 2021. *Highway safety analytics and modeling*. Elsevier.
- Mahmud, S.S., Ferreira, L., Hoque, M.S., Tavassoli, A., 2017. Application of proximal surrogate indicators for safety evaluation: A review of recent developments and research needs. *IATSS research* 41, 153–163.
- Mannering, F., Bhat, C.R., Shankar, V., Abdel-Aty, M., 2020. Big data, traditional data and the tradeoffs between prediction and causality in highway-safety analysis. *Analytic methods in accident research* 25, 100113.
- Minderhoud, M.M., Bovy, P.H., 2001. Extended time-to-collision measures for road traffic safety assessment. *Accident Analysis & Prevention* 33, 89–97.
- National Center for Statistics and Analysis, 2025. Early estimate of motor vehicle traffic fatalities in 2024. *Traffic Safety Facts Crash•Stats Brief Statistical Summary DOT HS 813 710*. National Highway Traffic Safety Administration.
- Nazir, F., Ali, Y., Sharma, A., Zheng, Z., Haque, M.M., 2023. Car-following crash risk analysis in a connected environment: A bayesian non-stationary generalised extreme value model. *Analytic methods in accident research* 39, 100278.
- Orsini, F., Gecchele, G., Gastaldi, M., Rossi, R., 2019. Collision prediction in roundabouts: a comparative study of extreme value theory approaches. *Transportmetrica A: transport science* 15, 556–572.
- Orsini, F., Gecchele, G., Gastaldi, M., Rossi, R., 2020. Large-scale road safety evaluation using extreme value theory. *IET Intelligent Transport Systems* 14, 1004–1012.
- Ozbay, K., Yang, H., Bartin, B., Mudigonda, S., 2008. Derivation and validation of new simulation-based surrogate safety measure. *Transportation research record* 2083, 105–113.
- Pei, X., Wong, S., Sze, N.N., 2011. A joint-probability approach to crash prediction models. *Accident Analysis & Prevention* 43, 1160–1166.
- Perkins, S.R., Harris, J.I., (1967). Traffic conflict characteristics: Freeway curve and exit area f1, december, 1966. *TRB* .
- Saunier, N., Sayed, T., 2008. Probabilistic framework for automated analysis of exposure to road collisions. *Transportation research record* 2083, 96–104.

- Singh, S., Ali, Y., Haque, M.M., 2024. A bayesian extreme value theory modelling framework to assess corridor-wide pedestrian safety using autonomous vehicle sensor data. *Accident Analysis & Prevention* 195, 107416.
- Singh, S., Ali, Y., Mannering, F., Haque, M.M., 2025. Autonomous vehicle sensor data and the estimation of network-wide spatiotemporal generalized extreme value models of rear-end injury-severity crash frequencies. *Analytic Methods in Accident Research*, 100390.
- Songchitruksa, P., Tarko, A.P., 2006. The extreme value theory approach to safety estimation. *Accident Analysis & Prevention* 38, 811–822.
- Spiegelhalter, D.J., Best, N.G., Carlin, B.P., Van Der Linde, A., 2002. Bayesian measures of model complexity and fit. *Journal of the royal statistical society: Series b (statistical methodology)* 64, 583–639.
- St-Aubin, P., Miranda-Moreno, L., Saunier, N., 2013. An automated surrogate safety analysis at protected highway ramps using cross-sectional and before–after video data. *Transportation Research Part C: Emerging Technologies* 36, 284–295.
- Sun, T., Segu, M., Postels, J., Wang, Y., Van Gool, L., Schiele, B., Tombari, F., Yu, F., 2022. Shift: a synthetic driving dataset for continuous multi-task domain adaptation, in: *Proceedings of the IEEE/CVF Conference on Computer Vision and Pattern Recognition*, pp. 21371–21382.
- Tahir, H.B., Haque, M.M., 2024. A non-stationary bivariate extreme value model to estimate real-time pedestrian crash risk by severity at signalized intersections using artificial intelligence-based video analytics. *Analytic Methods in Accident Research* 43, 100339.
- Tak, S., Kim, S., Yeo, H., 2015. Development of a deceleration-based surrogate safety measure for rear-end collision risk. *IEEE transactions on intelligent transportation systems* 16, 2435–2445.
- Tarko, A.P., 2012. Use of crash surrogates and exceedance statistics to estimate road safety. *Accident Analysis & Prevention* 45, 230–240.
- Tarko, A.P., 2018. Estimating the expected number of crashes with traffic conflicts and the lomax distribution—a theoretical and numerical exploration. *Accident Analysis & Prevention* 113, 63–73.
- Venthuruthiyil, S.P., Chunchu, M., 2022. Anticipated collision time (act): A two-dimensional surrogate safety indicator for trajectory-based proactive safety assessment. *Transportation research part C: emerging technologies* 139, 103655.
- Wang, C., Xu, C., Xia, J., Qian, Z., Lu, L., 2018. A combined use of microscopic traffic simulation and extreme value methods for traffic safety evaluation. *Transportation Research Part C: Emerging Technologies* 90, 281–291.
- Wang, T., Kim, S., Wenxuan, J., Xie, E., Ge, C., Chen, J., Li, Z., Luo, P., 2024. Deepaccident: A motion and accident prediction benchmark for v2x autonomous driving, in: *Proceedings of the AAAI Conference on Artificial Intelligence*, pp. 5599–5606.
- Washington, S., Karlaftis, M.G., Mannering, F., Anastasopoulos, P., 2020. Statistical and econometric methods for transportation data analysis. Chapman and Hall/CRC.
- Wilson, B., Qi, W., Agarwal, T., Lambert, J., Singh, J., Khandelwal, S., Pan, B., Kumar, R., Hartnett, A., Pontes, J.K., et al., 2023. Argoverse 2: Next generation datasets for self-driving perception and forecasting. *arXiv preprint arXiv:2301.00493*.
- Xu, R., Xiang, H., Xia, X., Han, X., Li, J., Ma, J., 2022. Opv2v: An open benchmark dataset and fusion pipeline for perception with vehicle-to-vehicle communication, in: *2022 International Conference on Robotics and Automation (ICRA)*, IEEE. pp. 2583–2589.
- Yu, H., Luo, Y., Shu, M., Huo, Y., Yang, Z., Shi, Y., Guo, Z., Li, H., Hu, X., Yuan, J., et al., 2022. Dair-v2x: A large-scale dataset for vehicle-infrastructure cooperative 3d object detection, in: *Proceedings of the IEEE/CVF Conference on Computer Vision and Pattern Recognition*, pp. 21361–21370.
- Yuan, J., Abdel-Aty, M., Gong, Y., Cai, Q., 2019. Real-time crash risk prediction using long short-term memory recurrent neural network. *Transportation research record* 2673, 314–326.
- Zhang, H., Liptrott, M., Bessis, N., Cheng, J., 2019. Real-time traffic analysis using deep learning techniques and uav based video, in: *2019 16th IEEE International Conference on Advanced Video and Signal Based Surveillance (AVSS)*, IEEE. pp. 1–5.
- Zheng, L., Huang, Y., Sayed, T., Wen, C., 2021a. Validating the bayesian hierarchical extreme value model for traffic conflict-based crash estimation on freeway segments with site-level factors. *Accident Analysis & Prevention* 159, 106269.
- Zheng, L., Ismail, K., Meng, X., 2014. Freeway safety estimation using extreme value theory approaches: A comparative study. *Accident Analysis & Prevention* 62, 32–41.
- Zheng, L., Sayed, T., 2019. From univariate to bivariate extreme value models: Approaches to integrate traffic conflict indicators for crash estimation. *Transportation research part C: emerging technologies* 103, 211–225.
- Zheng, L., Sayed, T., 2020. A novel approach for real time crash prediction at signalized intersections. *Transportation research part C: emerging technologies* 117, 102683.
- Zheng, L., Sayed, T., Essa, M., 2019. Bayesian hierarchical modeling of the non-stationary traffic conflict extremes for crash estimation. *Analytic methods in accident research* 23, 100100.
- Zheng, L., Sayed, T., Mannering, F., 2021b. Modeling traffic conflicts for use in road safety analysis: A review of analytic methods and future directions. *Analytic methods in accident research* 29, 100142.

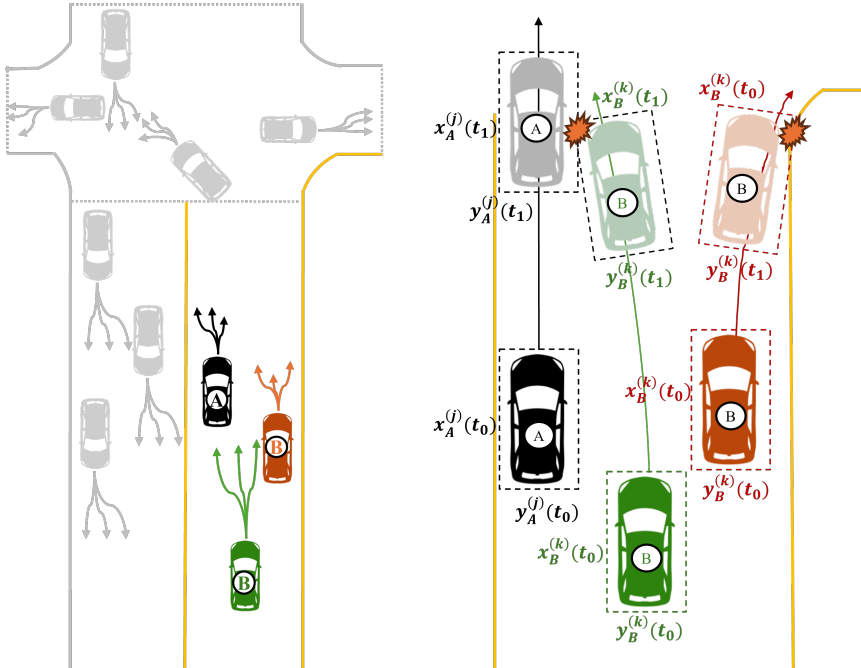


Fig. 1. Computation of 2D-TTC for near-miss scenarios

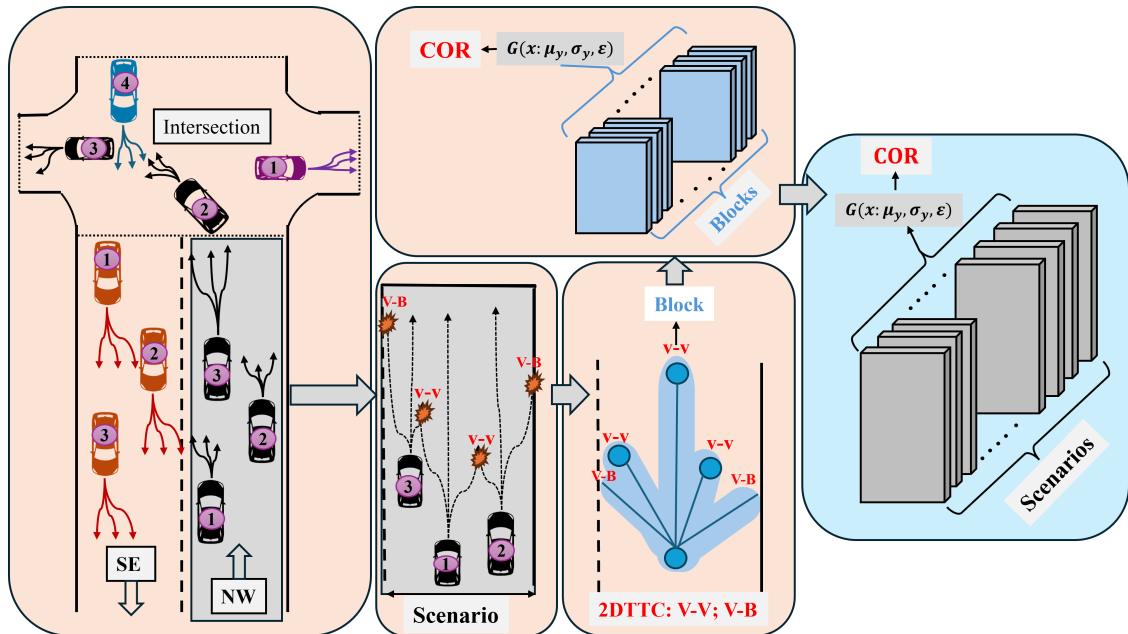


Fig. 2. COR time series generation

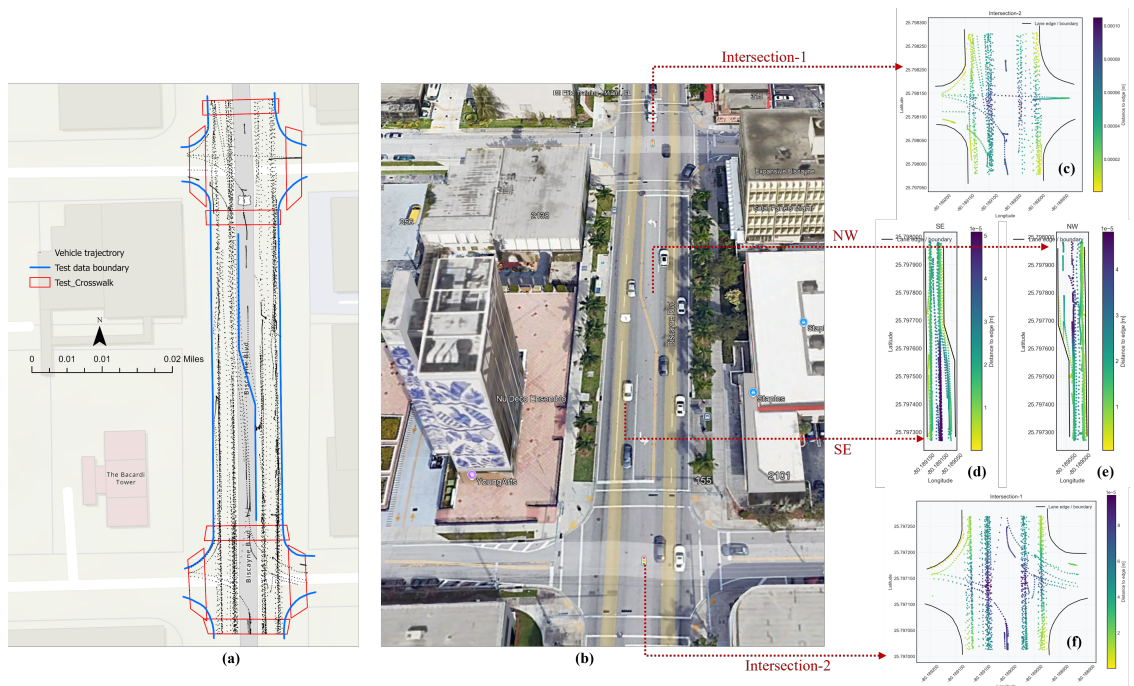


Fig. 3. AV data transformed to real-world coordinates and aligned: (a) trajectories with lane boundaries and crosswalks, (b) validation with satellite imagery, and (c–f) directional traffic patterns highlighting interaction hotspots.

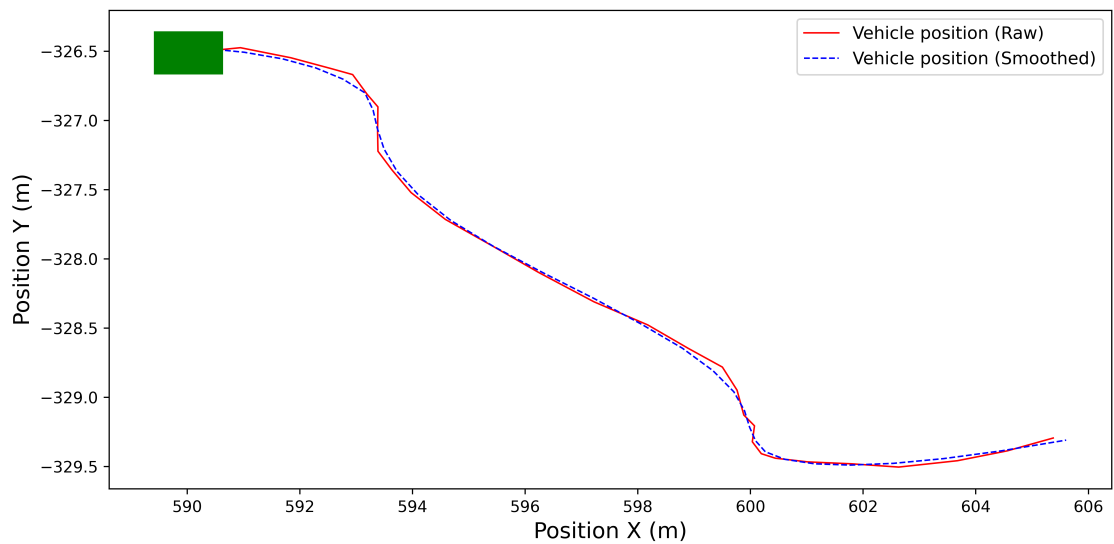


Fig. 4. Effect of B-spline smoothing on a sample trajectory, showing removal of noise while preserving geometric fidelity

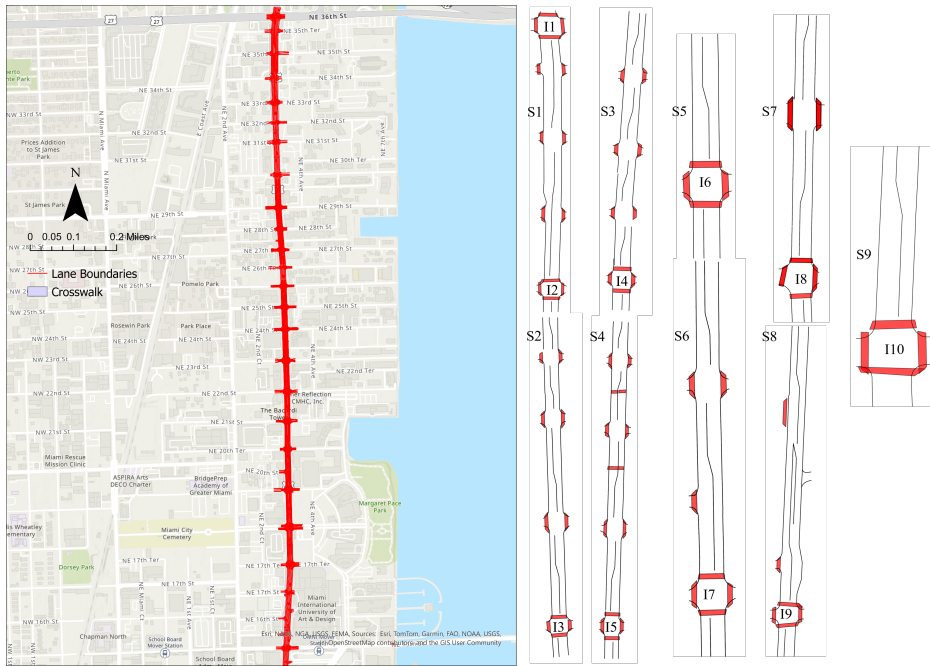


Fig. 5. Segmented study corridor along Biscayne Boulevard, Miami, with lane boundaries and crosswalks. Insets show direction-specific segments (S1–S9) and intersections (I1–I10)

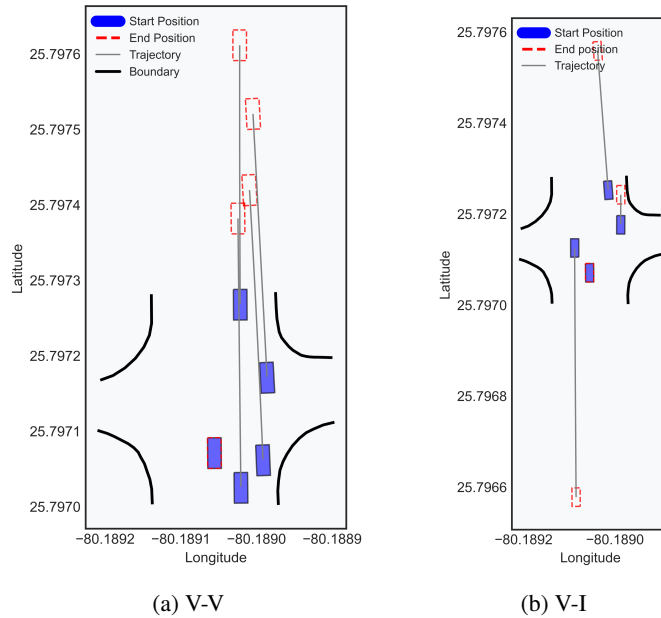


Fig. 6. Representative intersection-level near-miss detection using the 2D-TTC framework: (a) V–V and (b) V–I

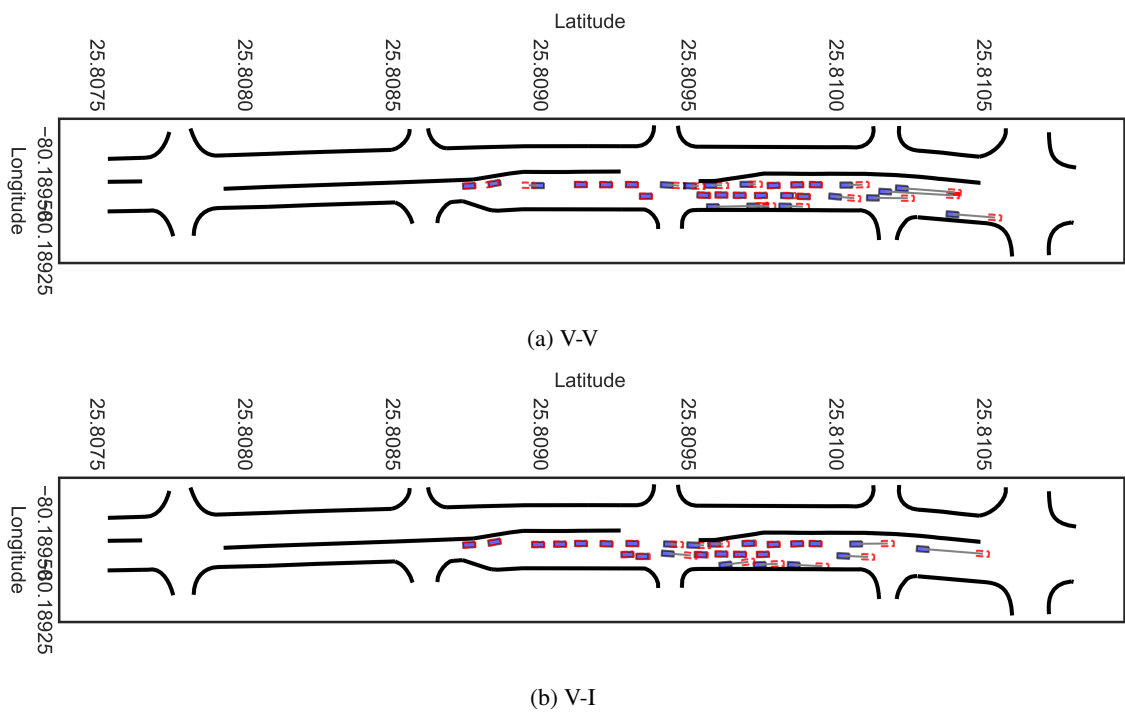
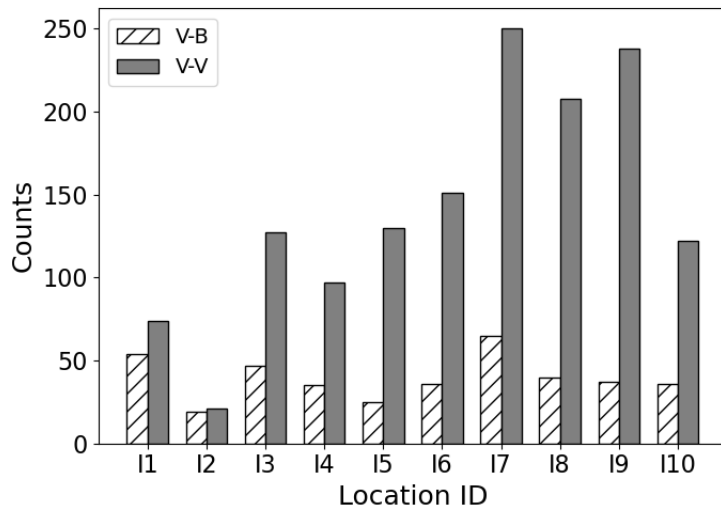
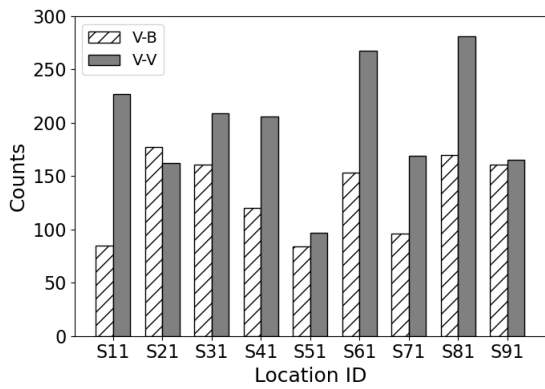


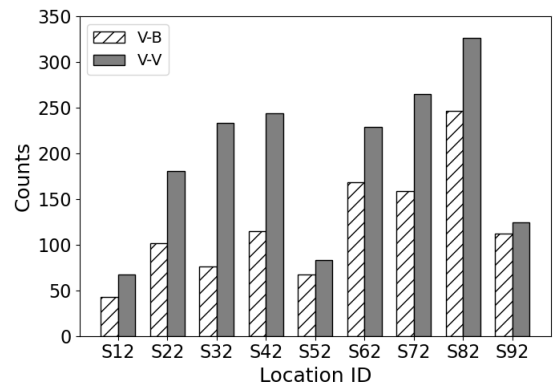
Fig. 7. Representative segment-level near-miss detection using the 2D-TTC framework: (a) V-V and (b) V-I



(a) Intersection



(b) Segment: NB



(c) Segment: SB

Fig. 8. BM near-miss frequencies by location type and direction

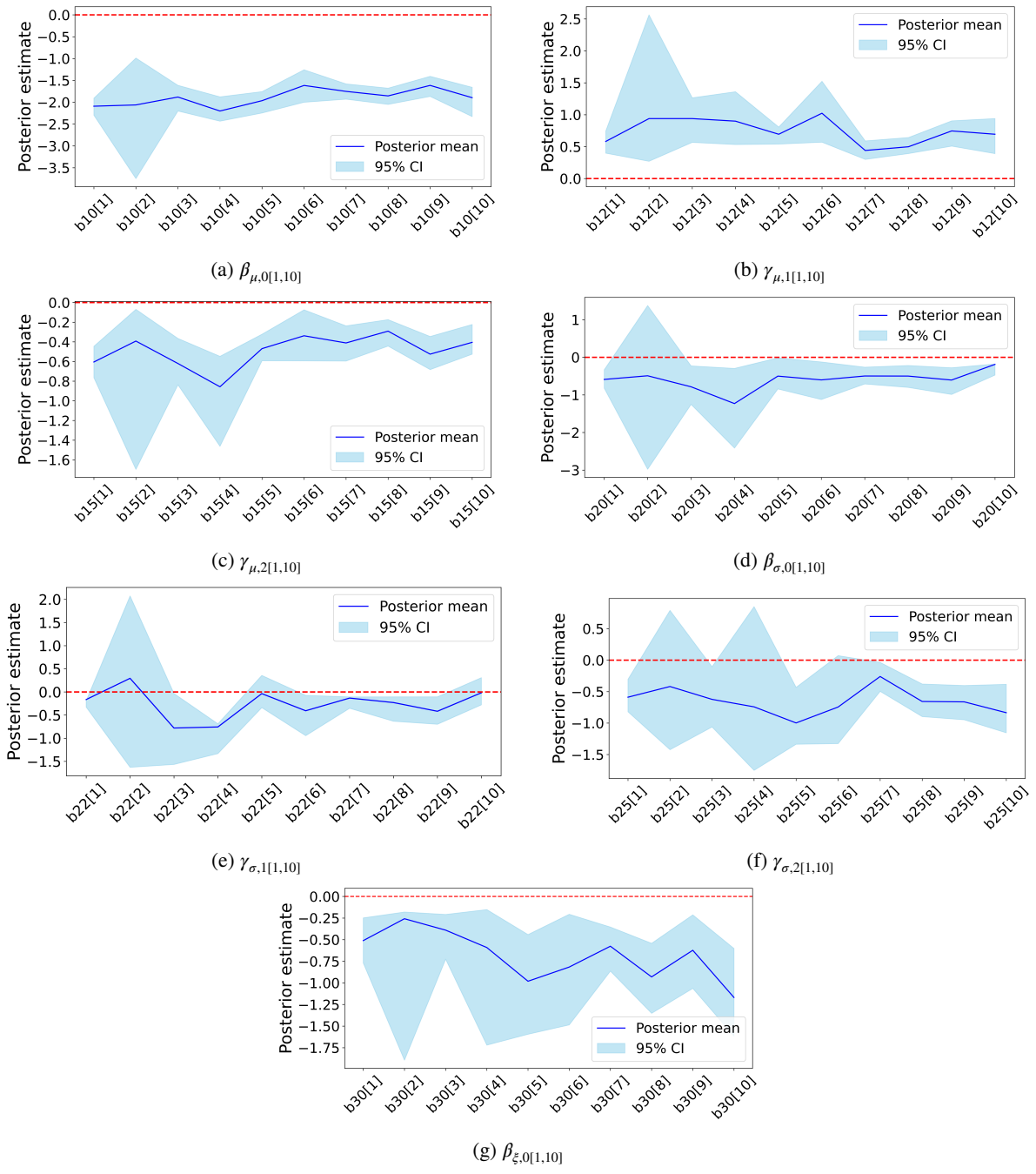


Fig. 9. Posterior estimates for V-V near-misses at intersections

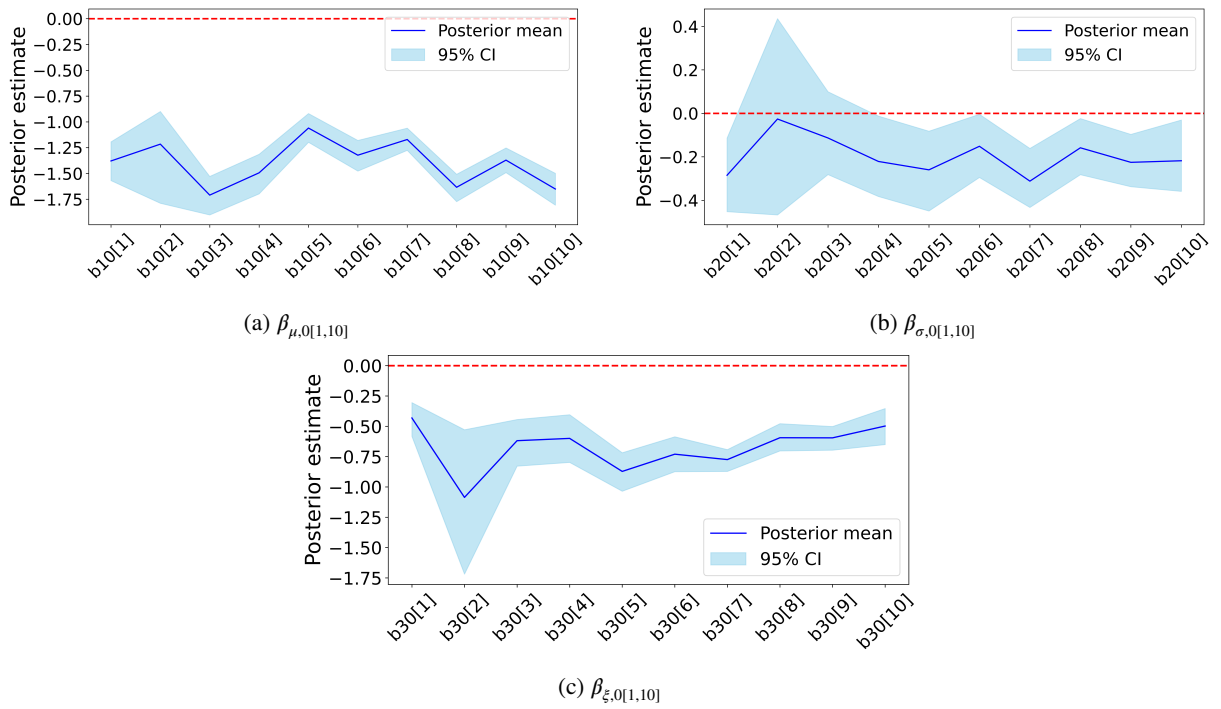


Fig. 10. Posterior estimates for V-I near-misses at intersections

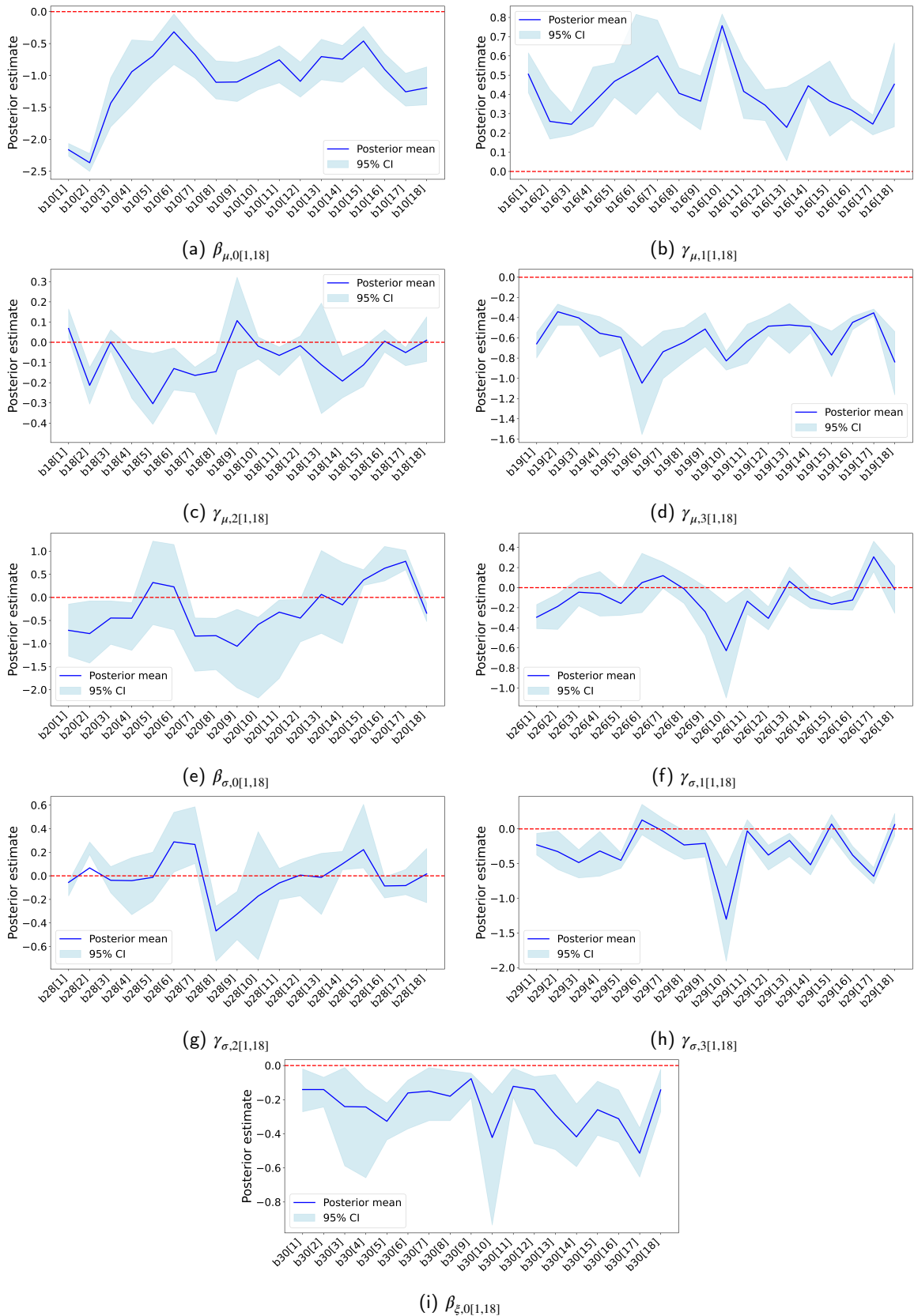


Fig. 11. Posterior estimates for V-V near-misses at segments

Table 7
Posterior estimates V-V near misses at segments

Model Parameters	Hyperparameter	Covariate	HBSFP			HBSGRP		
			Mean	SD ^a	95% CRI ^b	Mean	SD ^a	95% CRI ^b
<i>Location Parameter ($\mu_{k,i}$)</i>								
$\beta_{\mu,0}$	Fixed	Intercept	-2.117	0.032	[-2.181, -2.025] [†]	-	-	-
$\beta_{\mu,0,k}$	Random	Intercept	-	-	-	-1.047	0.171	[-1.369, -0.772] [†]
$\gamma_{\mu,1,k}$	Random	Relative speed	-	-	-	0.406	0.068	[0.286, 0.543] [†]
$\gamma_{\mu,2,k}$	Random	Relative deceleration	-	-	-	-0.082	0.016	[-0.197, -0.057] [†]
$\gamma_{\mu,3,k}$	Random	Relative distance	-	-	-	-0.600	0.082	[-0.779, -0.454] [†]
$\beta_{\mu,1}$	Fixed	Relative speed	0.446	0.037	[0.376, 0.519] [†]	-	-	-
$\beta_{\mu,2}$	Fixed	Relative acceleration	-0.068	0.017	[-0.154, -0.034] [†]	-0.079	0.037	[-0.163, -0.032] [†]
$\beta_{\mu,3}$	Fixed	Relative deceleration	-0.074	0.018	[-0.108, -0.040] [†]	-	-	-
$\beta_{\mu,4}$	Fixed	Relative distance	-0.669	0.063	[-0.801, -0.552] [†]	-	-	-
$\beta_{\mu,5}$	Fixed	Jerk	-0.004	0.001	[-0.007, -0.002] [†]	-0.156	0.043	[-0.234, -0.101] [†]
$\beta_{\mu,6}$	Fixed	Heading difference	0.043	0.016	[0.011, 0.073] [†]	0.044	0.008	[0.029, 0.059] [†]
$\beta_{\mu,7}$	Fixed	Steering difference	0.042	0.012	[0.018, 0.066] [†]	0.026	0.010	[0.007, 0.046] [†]
$\beta_{\mu,8}$	Fixed	Volume	0.035	0.013	[0.009, 0.060] [†]	0.019	0.008	[0.002, 0.038] [†]
$\beta_{\mu,9}$	Fixed	Lane no	-0.006	0.011	[-0.027, 0.015]	0.009	0.011	[-0.011, 0.032]
$\beta_{\mu,10}$	Fixed	Lane width	0.003	0.001	[0.001, 0.007] [†]	0.017	0.009	[0.002, 0.031] [†]
$\beta_{\mu,11}$	Fixed	Driveway density	-0.001	0.015	[-0.029, 0.027]	0.489	0.114	[0.256, 0.578] [†]
$\beta_{\mu,12}$	Fixed	Median (Undivided=1, else=0)	-0.004	0.033	[-0.070, 0.062]	-0.412	0.155	[-0.711, -0.070] [†]
$\beta_{\mu,13}$	Fixed	Vehicle position (Left lane=1, else=0)	0.029	0.038	[-0.048, 0.103]	0.055	0.006	[0.012, 0.105] [†]
<i>Scale Parameter ($\log \sigma_{k,i}$)</i>								
$\beta_{\sigma,0}$	Fixed	Intercept	-0.622	0.045	[-0.711, -0.533] [†]	-	-	-
$\beta_{\sigma,0,k}$	Random	Intercept	-	-	-	-0.253	0.047	[-0.952, -0.156] [†]
$\gamma_{\sigma,1,k}$	Random	Relative speed	-	-	-	-0.055	0.026	[-0.107, -0.003] [†]
$\gamma_{\sigma,2,k}$	Random	Relative deceleration	-	-	-	-0.119	0.018	[-0.154, -0.084] [†]
$\gamma_{\sigma,3,k}$	Random	Relative distance	-	-	-	-0.304	0.117	[-0.520, -0.084] [†]
$\beta_{\sigma,1}$	Fixed	Relative speed	-0.116	0.050	[-0.217, -0.023] [†]	-	-	-
$\beta_{\sigma,2}$	Fixed	Relative acceleration	-0.611	0.097	[-0.817, -0.439] [†]	-0.024	0.173	[-0.277, 0.298]
$\beta_{\sigma,3}$	Fixed	Relative deceleration	-0.060	0.019	[-0.097, -0.024] [†]	-	-	-
$\beta_{\sigma,4}$	Fixed	Relative distance	0.003	0.064	[-0.121, 0.130]	-	-	-
$\beta_{\sigma,5}$	Fixed	Jerk	0.006	0.000	[0.004, 0.008] [†]	0.357	0.147	[0.061, 0.611] [†]
$\beta_{\sigma,6}$	Fixed	Heading difference	0.065	0.017	[0.032, 0.099] [†]	0.033	0.011	[0.017, 0.068] [†]
$\beta_{\sigma,7}$	Fixed	Steering difference	0.011	0.016	[-0.020, 0.043]	-0.001	0.019	[-0.031, 0.029]
$\beta_{\sigma,8}$	Fixed	Volume	-0.011	0.016	[-0.043, 0.020]	-0.012	0.015	[-0.030, 0.029]
$\beta_{\sigma,9}$	Fixed	Lane no	-0.031	0.014	[-0.049, -0.005] [†]	-0.028	0.017	[-0.061, -0.002] [†]
$\beta_{\sigma,10}$	Fixed	Lane width	-0.006	0.003	[-0.012, -0.000] [†]	-0.015	0.009	[-0.044, -0.001] [†]
$\beta_{\sigma,11}$	Fixed	Driveway density	0.040	0.018	[0.004, 0.075] [†]	0.284	0.215	[0.019, 0.648] [†]
$\beta_{\sigma,12}$	Fixed	Median (Undivided=1, else=0)	0.076	0.042	[-0.006, 0.158]	-0.205	0.095	[-0.369, -0.058] [†]
$\beta_{\sigma,13}$	Fixed	Vehicle position (Left lane=1, else=0)	-0.049	0.052	[-0.156, 0.051]	-0.109	0.052	[-0.209, -0.006] [†]
<i>Shape Parameter ($\xi_{k,i}$)</i>								
$\beta_{\xi,0}$	Fixed	Intercept	-0.116	0.030	[-0.178, -0.059] [†]	-	-	-
$\beta_{\xi,0,k}$	Random	Intercept	-	-	-	-0.185	0.144	[-0.436, -0.163] [†]
<i>Model Fit</i>								
DIC				4528			4189	
WAIC				4594			4276	
LOOIC				4608.25			4278	

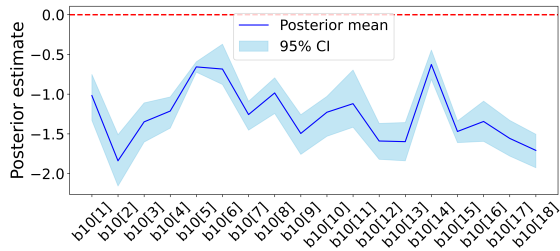
HBSFP Hierarchical Bayesian Spatial Fixed Parameter
HBSGRP Hierarchical Bayesian Spatial Grouped Random Parameter

^a Standard deviation

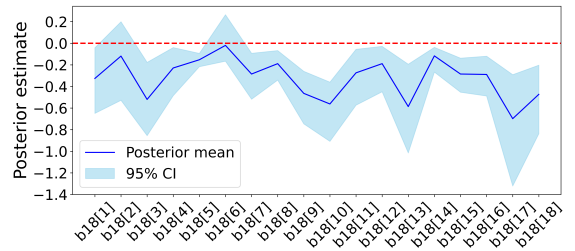
^b 95% Bayesian credible interval

- Covariate not included in the model

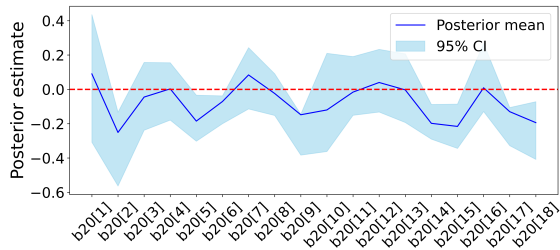
[†] Indicates statistical significance at the 95% level (interval excludes 0)



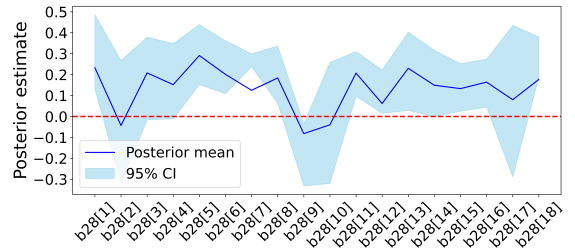
(a) $\beta_{\mu,0[1,18]}$



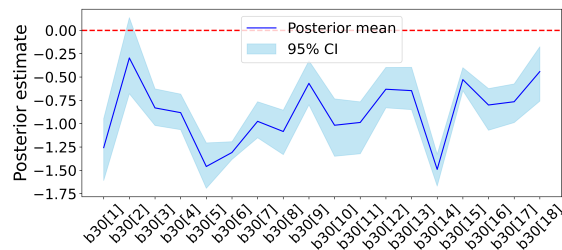
(b) $\gamma_{\mu,1[1,18]}$



(c) $\beta_{\sigma,0[1,18]}$



(d) $\gamma_{\sigma,1[1,18]}$



(e) $\beta_{\xi,0[1,18]}$

Fig. 12. Posterior estimates V-I near misses at segments

Table 8
Posterior estimates V-I near misses at segments

Model Parameters	Hyperparameter	Covariate	HBSFP			HBSGRP		
			Mean	SD ^a	95% CRI ^b	Mean	SD ^a	95% CRI ^b
<i>Location Parameter ($\mu_{k,i}$)</i>								
$\beta_{\mu,0}$	Fixed	Intercept	-1.287	0.037	[-1.352, -1.22] [†]	-	-	-
$\beta_{\mu,0,k}$	Random	Intercept	-	-	-	-1.263	0.122	[-1.494, -1.037] [†]
$\gamma_{\mu,1,k}$	Random	Relative distance	-	-	-	-0.317	0.148	[-0.632, -0.104] [†]
$\beta_{\mu,1}$	Fixed	Relative speed	-0.027	0.018	[-0.061, -0.008] [†]	0.009	0.001	[0.006, 0.027] [†]
$\beta_{\mu,2}$	Fixed	Relative acceleration	8.36E-04	0.019	[-0.045, 0.036]	0.025	0.013	[0.002, 0.057] [†]
$\beta_{\mu,3}$	Fixed	Relative deceleration	-0.039	0.008	[-0.098, -0.004] [†]	-0.032	0.008	[-0.087, -0.014] [†]
$\beta_{\mu,4}$	Fixed	Relative distance	-0.257	0.025	[-0.304, -0.207] [†]	-	-	-
$\beta_{\mu,5}$	Fixed	Jerk	-0.124	0.069	[-0.224, 0.289]	-0.074	0.039	[-0.124, 0.202]
$\beta_{\mu,6}$	Fixed	Heading difference	0.025	0.025	[-0.025, 0.069]	0.027	0.014	[0.001, 0.049] [†]
$\beta_{\mu,7}$	Fixed	Steering difference	0.033	0.017	[0.004, 0.065] [†]	0.041	0.016	[0.003, 0.066] [†]
$\beta_{\mu,8}$	Fixed	Volume	-0.002	0.007	[-0.016, 0.010]	0.043	0.021	[0.015, 0.084] [†]
$\beta_{\mu,9}$	Fixed	Lane no	-0.001	0.012	[-0.019, 0.016]	0.042	0.021	[0.004, 0.078] [†]
$\beta_{\mu,10}$	Fixed	Lane width	-0.027	0.018	[-0.061, -0.008] [†]	0.013	0.009	[0.000, 0.032] [†]
$\beta_{\mu,11}$	Fixed	Driveway density	-0.007	0.024	[-0.057, 0.042]	-0.237	0.105	[-0.403, -0.020] [†]
$\beta_{\mu,12}$	Fixed	Median (Undivided=1, else=0)	-0.644	0.102	[-0.773, -0.513] [†]	-0.083	0.059	[-0.196, -0.019] [†]
$\beta_{\mu,13}$	Fixed	Vehicle position (Left lane=1, else=0)	0.057	0.033	[0.028, 0.091] [†]	-0.064	0.014	[-0.082, -0.038] [†]
<i>Scale Parameter ($\log \sigma_{k,i}$)</i>								
$\beta_{\sigma,0}$	Fixed	Intercept	-0.495	0.156	[-0.703, -0.303] [†]	-	-	-
$\beta_{\sigma,0,k}$	Random	Intercept	-	-	-	-0.076	0.104	[-0.265, 0.083] [†]
$\gamma_{\sigma,1,k}$	Random	Relative distance	-	-	-	0.135	0.103	[0.011, 0.318] [†]
$\beta_{\sigma,1}$	Fixed	Relative speed	0.039	0.016	[0.012, 0.061] [†]	0.013	0.001	[0.004, 0.038] [†]
$\beta_{\sigma,2}$	Fixed	Relative acceleration	0.002	0.017	[-0.030, 0.042]	-0.026	0.014	[-0.064, -0.001] [†]
$\beta_{\sigma,3}$	Fixed	Relative deceleration	-0.036	0.013	[-0.075, -0.014] [†]	-0.048	0.021	[-0.089, -0.022] [†]
$\beta_{\sigma,4}$	Fixed	Relative distance	0.167	0.018	[0.136, 0.199] [†]	-	-	-
$\beta_{\sigma,5}$	Fixed	Jerk	-0.108	0.054	[0.452, -0.119]	-0.078	0.119	[-0.312, 0.078]
$\beta_{\sigma,6}$	Fixed	Heading difference	-0.019	0.020	[-0.053, 0.020]	-0.029	0.017	[-0.049, -0.001] [†]
$\beta_{\sigma,7}$	Fixed	Realative steering angle	-0.033	0.012	[-0.065, -0.001] [†]	-0.032	0.024	[-0.059, -0.003] [†]
$\beta_{\sigma,8}$	Fixed	Volume	-0.007	0.018	[-0.039, 0.027]	0.001	0.016	[-0.026, 0.030]
$\beta_{\sigma,9}$	Fixed	Lane no	-0.028	0.017	[-0.058, -0.006] [†]	-0.021	0.012	[-0.046, -0.002] [†]
$\beta_{\sigma,10}$	Fixed	Lane width	-0.010	0.020	[-0.044, 0.030]	0.018	0.016	[0.010, 0.045] [†]
$\beta_{\sigma,11}$	Fixed	Driveway density	0.016	0.019	[-0.021, 0.055]	-0.125	0.028	[-0.239, 0.018]
$\beta_{\sigma,12}$	Fixed	Median (Undivided=1, else=0)	0.663	0.166	[0.440, 0.880] [†]	0.174	0.090	[0.263, 0.553] [†]
$\beta_{\sigma,13}$	Fixed	Vehicle position (Left lane=1, else=0)	-0.046	0.027	[-0.080, -0.012] [†]	0.055	0.010	[0.039, 0.071] [†]
<i>Shape Parameter ($\xi_{k,i}$)</i>								
$\beta_{\xi,0}$	Fixed	Intercept	-0.845	0.028	[-0.897, -0.788] ^{†g}	-	-	-
$\beta_{\xi,0,k}$	Random	Intercept	-	-	-	-0.887	0.118	[-1.123, -0.659] [†]
<i>Model Fit</i>								
DIC			6760			6550		
WAIC			6775			6595		
LOOIC			6791.2			6601		

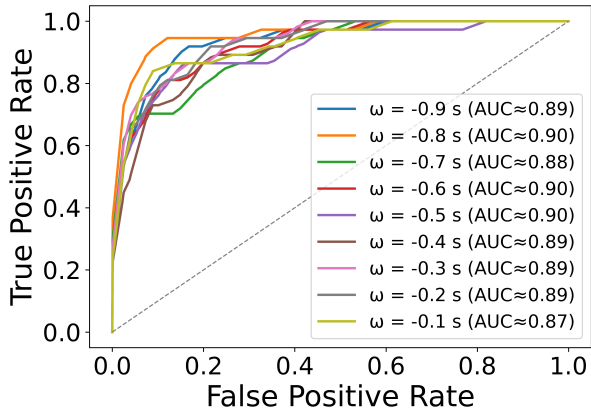
HBSFP Hierarchical Bayesian Spatial Fixed Parameter
HBSGRP Hierarchical Bayesian Spatial Grouped Random Parameter

^a Standard deviation

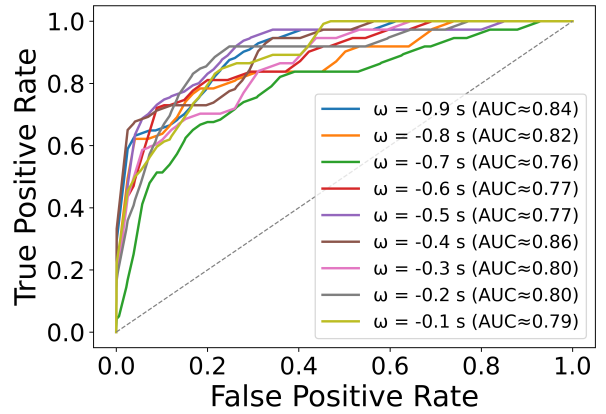
^b 95% Bayesian credible interval

- Covariate not included in the model

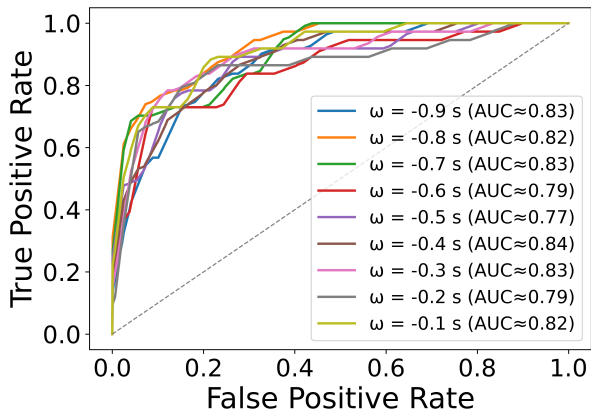
[†] Indicates statistical significance at the 95% level (interval excludes 0)



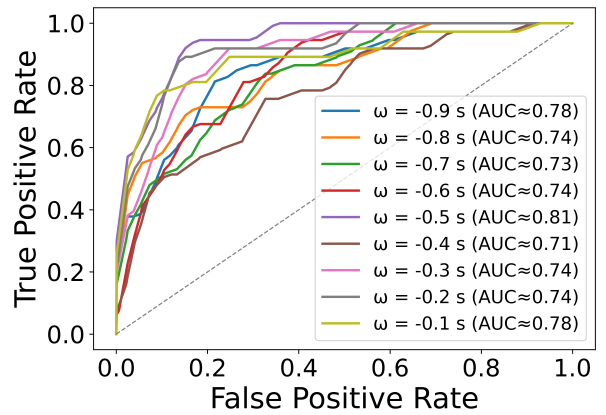
(a) V-V Segment



(b) V-I Segment



(c) V-V Intersection



(d) V-I Intersection

Fig. 13. ROC curves for four HBSGRP-UGEV models across severity thresholds from $\omega = -0.1$ s to $\omega = -0.9$ s